Relating Darcy-scale chemical reaction order to pore-scale spatial heterogeneity

Po-Wei Huang[1], Bernd Flemisch[2], Chao-Zhong Qin[3], Martin O. Saar[1,4], Anozie Ebigbo[1,5]

[1]Geothermal Energy and Geofluids Group, Institute of Geophysics, Department of Earth Sciences, ETH Zurich, Zurich, Switzerland
[2]Institute for Modelling Hydraulic and Environmental Systems, University of Stuttgart, Stuttgart, Germany
[3]State Key Laboratory of Coal Mine Disaster Dynamics and Control, Chongqing University, Chongqing, China
[4]Department of Earth and Environmental Sciences, University of Minnesota, Minneapolis, USA
[5]Hydromechanics Research Group, Helmut Schmidt University, Hamburg, Germany

Key Points:

- We derive relationships between raw moments of pore-size, effective surface area distributions and the Darcy-scale reaction order.
- The Darcy-scale reaction order, independent of Péclet and Damköhler numbers, serves as a constitutive relation for Darcy-scale modeling.
- We use simulations of flow-through experiments at both lab and field scales to demonstrate the utility of the constitutive relation.

Corresponding author: Po-Wei Huang, powei.huang@erdw.ethz.ch

Corresponding author: Anozie Ebigbo, ebigbo@hsu-hh.de

Abstract

Due to spatial scaling effects, there is a discrepancy in mineral dissolution rates in porous media measured at different spatial scales. Many reasons for this spatial scaling effect can be given. We investigate one such reason, i.e. how pore-scale spatial heterogeneity in porous media affects overall mineral dissolution rates. Using the bundle-of-tubes model as an analogy for porous media, we show that the Darcy-scale reaction order increases as the statistical similarity between the pore sizes and the effective-surface-area ratio of the porous sample decreases. The analytical results quantify mineral spatial heterogeneity using the Darcy-scale reaction order and give a mechanistic explanation to the usage of reaction order in Darcy-scale modeling. The relation is used as a constitutive relation of reactive transport at the Darcy scale. We test the constitutive relation by simulating flow-through experiments. The proposed constitutive relation is able to model the solute breakthrough curve of the simulations. In addition, our results imply that we can infer mineral spatial heterogeneity of a porous medium using measured solute concentration over time in a flow-through dissolution experiment.

1 Introduction

Geochemical reactions such as mineral dissolution play an essential role in determining water chemistry, soil formation, biogeochemical cycling, and global climate (Wen & Li, 2017). Mineral reactions can also occur during injection of CO_2 in groundwater reservoirs (Ebigbo et al., 2012; Buscheck et al., 2014; Pogge von Strandmann et al., 2019). One of the most significant obstacles to understanding the geochemical reactivity of natural subsurface environments stems from the multitude of spatial scales that have to be considered (Noiriel et al., 2012). Due to spatial scaling effects, mineral dissolution rates are known to be 3–6 orders of magnitude lower in the field than when measured in the laboratory (White & Brantley, 2003; Navarre-Sitchler & Brantley, 2007; Maher, 2010; Moore et al., 2012). The deviation in mineral dissolution rates strongly limits the extrapolation of kinetic dissolution models and parameters characterized in the laboratory to natural systems (R. Li et al., 2020).

Many factors are responsible for the spatial scaling effects of mineral dissolution rates. This work focuses on how pore-size distribution—which contributes to hydraulic heterogeneity—and spatial mineral distribution cause such spatial scaling effects. L. Li et al. (2007) performed simulations with various settings of spatial mineral distribution and concluded that spatial mineral distribution has a significant scaling effect when the reactive minerals are of small but typical proportions. Experimental studies using a column packed with quartz and magnesite have confirmed the significant role of spatial heterogeneities in subsurface reactive transport and can be used to quantify the effect of spatial mineral distribution on dissolution rates (L. Li et al., 2013, 2014; L. Li & Salehikhoo, 2015). X-ray micro-tomography provides observations of the impact of physical and chemical heterogeneity on reaction rates in multimineral porous media (Al-Khulaifi et al., 2017, 2018, 2019; Menke et al., 2016, 2018). Fischer et al. (2014) and Fischer and Luttge (2017) studied how mineral surface roughness at the nanometer scale affects surface reaction rates and proposed to upscale the mineral reaction rate using Monte-Carlo simulations. Ma et al. (2021) quantified the accessible surface area of minerals in a sandstone using scanning electron microscopy (SEM) images and Brunauer-Emmett-Teller (BET) surface area measurements.

Regarding the influence of hydraulic heterogeneity, Wen and Li (2017) and Jung and Navarre-Sitchler (2018a) performed reactive transport simulations on stochastically generated permeability fields and studied how hydrologic heterogeneity affects mineral dissolution rates. Using Monte-Carlo simulations, Jung and Navarre-Sitchler (2018b) further studied the time dependency of mineral dissolution rates, and Wen

and Li (2018) developed an upscaled rate law for mineral dissolution in heterogeneous media under variable residence-time and length-scale conditions. R. Li et al. (2020) upscaled mineral dissolution rates in a porous medium with a random permeability field using the fluid travel-time distribution function. The works mentioned above used the transition state theory (Lasaga, 1998) to model mineral dissolution rates, with a macro-scale reaction order of unity ($n = 1$). This is reasonable since there are no physical explanations why this macro-scale reaction order should not be one (Lasaga, 1998; Brantley & Conrad, 2008).

However, there are rate models with a macro-scale reaction order of 2 in kinetics of crystal growth (Nancollas, 1968; Reddy, 1975, 1977). Such second-order kinetics are used for modeling surface spiral growth (A. E. Nielsen, 1984; Teng et al., 2000). Considering calcite as our mineral of particular interest, fitting experimental data using a reaction order larger than 1 is common, especially when the saturation is close to equilibrium (Plummer & Wigley, 1976; Plummer et al., 1978; Palmer, 1991; Svensson & Dreybrodt, 1992). A higher reaction order is also observed in modeling calcite dissolution in seawater (e.g., Subhas et al., 2015; Naviaux et al., 2019).

In this work, we use analytical techniques to develop a constitutive relation of mineral dissolution kinetics in porous media based on models with a reaction order $n > 1$. We characterize hydraulic heterogeneity and mineral spatial heterogeneity by the longitudinal dispersivity and the reaction order. We use the bundle-of-tubes analogy to show how the reaction order relates to both hydraulic and spatial mineral heterogeneity in porous media. Furthermore, we simulate experimental scenarios involving advective and dispersive transport using such a constitutive relation. Our results show how concentration breakthrough curves of the reactive species reveal information of both the hydraulic and chemical heterogeneity of porous media.

2 Materials and methods

This section first introduces reactive transport models at the pore scale and the Darcy scale. Then we lay out statistical distributions of pore sizes and effective-surface-area ratios. Such distributions can thus define the volume-averaged concentration. Constitutive relations based on the Darcy-scale reaction order is established using Taylor series expansions. We check the applicability of the constitutive relations by comparing the modeled concentration and the volume-averaged concentration using a goodness of fit measure, the Jensen Shannon divergence. Finally, we explain how one can apply the proposed constitutive relation using a flow-through experiment.

2.1 Reactive transport at the pore scale

We use the advection-diffusion-reaction equation to model reactive transport at the pore scale. Consider an elongated pore such that the concentration of the mineral-forming solute can be approximated by a one-dimensional (1D) expression:

$$\frac{\partial C^*}{\partial t^*} + u\frac{\partial C^*}{\partial z^*} - D\frac{\partial^2 C^*}{\partial z^{*2}} = q, \tag{1}$$

where C^* is the solute concentration in the fluid, u is the fluid velocity, D is the molecular diffusivity of the solute, and q is the source term defined by a mineral dissolution model. A common mineral dissolution model is of second order:

$$q = \frac{A}{V_\mathrm{f}}(k_\mathrm{d} - k_\mathrm{p}C^{*2}), \tag{2}$$

where A is the mineral surface area, V_f is the fluid volume, k_d is the dissolution rate constant, and k_p is the precipitation rate constant. We relate the dissolution model with a more prevalent formulation involving the solubility product, K_sp, and the ion

activity product, IAP:

$$R_{\mathrm{dis}} = q\frac{V_{\mathrm{f}}}{A} = k_{\mathrm{d}}\left(1 - \frac{\mathrm{IAP}}{K_{\mathrm{sp}}}\right), \tag{3}$$

where R_{dis} is the mineral dissolution rate. One can switch between the two forms by stating IAP $= C^2$ and $K_{\mathrm{sp}} = k_{\mathrm{d}}/k_{\mathrm{p}}$. The statement, IAP $= C^2$ means the two mineral-forming ions have equal concentration, which arises from the assumption of electroneutrality of ions close to the mineral surface (Levenson & Emmanuel, 2013). We relate the dimensional and nondimensional quantities by

$$t^* = [t]\,t,\ z^* = L\,z,\ C^* = [C]\,C, \tag{4}$$

and we nondimensionalize equations (1) and (2) by the following scaling of time and concentration

$$[t] = \frac{L^2}{D}, \quad [C] = \sqrt{\frac{k_{\mathrm{d}}}{k_{\mathrm{p}}}}, \tag{5}$$

where L is a characteristic length. The variables in square brackets refer to characteristic quantities. Thus we have a nondimensional equation of reactive transport

$$\frac{\partial C}{\partial t} + Pe\,\frac{\partial C}{\partial z} - \frac{\partial^2 C}{\partial z^2} = Da(1 - C^2), \tag{6}$$

$$Pe = \frac{uL}{D}, \quad Da = \frac{A}{V_{\mathrm{f}}}\frac{L^2\sqrt{k_{\mathrm{d}}k_{\mathrm{p}}}}{D}. \tag{7}$$

where Pe is the Péclet number and Da is the Damköhler number.

First-order-kinetics models are uncommon, since chemical reactions often involve two reagents (Cussler, 2009). If one wanted to make use of first-order kinetics, one would have to assume the concentration of a mineral-forming ion is in excess or constant (Meile & Tuncay, 2006) or limit the usage of first-order kinetics to low solute concentrations (Kaufmann & Dreybrodt, 2007). Nonetheless, we introduce the model of first-order mineral dissolution kinetics,

$$q = \frac{A}{V_{\mathrm{f}}}(k_{\mathrm{d}} - k_{\mathrm{p}}C^*). \tag{8}$$

Combining equations (1) and (8), we scale time and concentration by

$$[t] = \frac{L^2}{D}, \quad [C] = \frac{k_{\mathrm{d}}}{k_{\mathrm{p}}}, \tag{9}$$

such that the Péclet and the Damköhler numbers are

$$Pe = \frac{uL}{D}, \quad Da = \frac{A}{V_{\mathrm{f}}}\frac{L^2 k_{\mathrm{p}}}{D}. \tag{10}$$

The nondimensional model of first-order reactive transport is therefore

$$\frac{\partial C}{\partial t} + Pe\,\frac{\partial C}{\partial z} - \frac{\partial^2 C}{\partial z^2} = Da(1 - C). \tag{11}$$

We define the velocity in a pore using the Hagen-Poiseuille equation,

$$u = \frac{r^2}{8}\frac{\Delta P}{\eta L_z}, \tag{12}$$

where r is the pore radius, η is the dynamic viscosity of the fluid, ΔP is the pressure difference between the inlet and the outlet, and L_z is the pore length.

2.2 Reactive transport at the Darcy scale

We use the bundle-of-tubes analogy to model reactive transport at the Darcy scale (Kozeny, 1927). We define the specific mineral surface area of the porous medium as

$$S = \frac{A}{V} = \frac{2L_z\pi\sum_{i=1}^{N}\omega_i r_i}{V}, \tag{13}$$

where V is the bulk volume of the porous medium, ω is the ratio between mineral surface area and the total surface area of a pore, and N is the total number of pores. We assume that the pores have the same length, L_z, as the porous medium, such that the tortuosity is 1. The porosity of the porous medium is

$$\phi = \frac{V_\mathrm{f}}{V} = \frac{L_z\pi\sum_{i=1}^{N}(r_i)^2}{V}. \tag{14}$$

Dividing equation (13) by equation (14), we obtain

$$\frac{S}{\phi} = \frac{A}{V_\mathrm{f}} = \frac{2\sum_{i=1}^{N}\omega_i r_i}{\sum_{i=1}^{N}(r_i)^2}. \tag{15}$$

Recall the Damköhler number for first-order kinetics, equation (10), the Damköhler number at the Darcy scale is

$$Da_\mathrm{d} = \frac{S}{\phi}\frac{L_z^2 k_\mathrm{p}}{D}, \tag{16}$$

where the characteristic length, L, is chosen to be the length of the porous medium, L_z. The Darcy-scale Damköhler number for second-order kinetics is

$$Da_\mathrm{d} = \frac{S}{\phi}\frac{L_z^2\sqrt{k_\mathrm{d}k_\mathrm{p}}}{D}. \tag{17}$$

Since we consider the porous medium as a bundle of tubes, the seepage velocity of the porous medium can be defined using a volume-averaged velocity,

$$\bar{u} = \frac{\sum_{i=1}^{N}u_i(r_i)^2}{\sum_{i=1}^{N}(r_i)^2} = \frac{\sum_{i=1}^{N}(r_i)^4}{8\sum_{i=1}^{N}(r_i)^2}\frac{\Delta P}{\mu L_z}. \tag{18}$$

Hence, the Péclet number at the Darcy scale is

$$Pe_\mathrm{d} = \frac{\bar{u}L_z}{D}. \tag{19}$$

Dispersion effects arise when the pore sizes are not uniform (Carbonell, 1979; Arriaza & Ghezzehei, 2013; Meng & Yang, 2017). Therefore, we introduce a longitudinal dispersion coefficient,

$$D_\mathrm{L} = \alpha_\mathrm{L}\bar{u}, \tag{20}$$

where α_L is the longitudinal dispersivity with the unit of length. We derived the longitudinal dispersion coefficient using the spatial moments of the averaged solute concentration of the bundle of tubes model,

$$D_\mathrm{L} = \bar{u}^2 t\left(\frac{\sum_{i=1}^{N}(r_i)^6\sum_{i=1}^{N}(r_i)^2}{\left(\sum_{i=1}^{N}(r_i)^4\right)^2} - 1\right) = \bar{u}^2 t\, f(r). \tag{21}$$

The shape factor, $f(r)$, abbreviates the expression of pore sizes in equation (21). Detailed derivations are presented in Appendix A. The longitudinal dispersivity is

$$\alpha_\mathrm{L} = \bar{u}t\, f(r) = \bar{z}\, f(r), \tag{22}$$

where $\bar{z}$ is the center of mass of an instantaneous source injected in the porous domain. The spatial moment analysis showed that the longitudinal dispersivity increases linearly as the distance traveled of an instantaneous source, which is reasonable in an infinite domain. In recent studies based on pore-network modeling, Mahmoodlu et al. (2020) observed the longitudinal dispersivity increases as travel distance increases.

By scaling the longitudinal dispersion coefficient by the molecular diffusivity yields the nondimensional reactive transport model at the Darcy scale,

$$\frac{\partial C}{\partial t} + Pe_{\mathrm{d}} \frac{\partial C}{\partial z} - \left(1 + (Pe_{\mathrm{d}})^2 t\, f(r)\right) \frac{\partial^2 C}{\partial z^2} = q_{\mathrm{d}}, \tag{23}$$

where q_{d} is the reaction term that is yet to be defined. Note that when all pores have the same radius and effective-surface-area ratio, equation (23) reduces to the equation for a single pore, equation (6). In the next section, we discuss statistical distributions of pore sizes and effective-surface-area ratios.

2.3 Statistical distributions of pore sizes and effective-surface-area ratios

The pore sizes of porous media usually follow a log-normal distribution (Shi et al., 1991; Hefny et al., 2020). The probability density function of a log-normally distributed variable, r, is

$$p(r) = \frac{1}{\sigma r \sqrt{2\pi}} \exp\left(-\frac{(\log(r) - \mu)^2}{2\sigma^2}\right), \tag{24}$$

where μ and σ are the mean and standard deviation of the variable's natural logarithm, respectively. The sum of pore sizes raised to the power of m can be described by a raw statistical moment,

$$\frac{1}{N}\sum_{i=1}^{N}(r_i)^m = \mathrm{E}(r^m) = \int_0^\infty r^m p(r) dr. \tag{25}$$

If the pore-size distribution is known, the permeability, k, of the bundle can be calculated as

$$k = \frac{\sum_{i=1}^{N}(r_i)^4}{8\sum_{i=1}^{N}(r_i)^2} = \frac{\mathrm{E}(r^4)}{8\mathrm{E}(r^2)}. \tag{26}$$

Using the moments of the lognormal distribution, we can now clarify the shape factor,

$$f(r) = \exp(4\sigma^2) - 1. \tag{27}$$

Since we are interested in not only the pore-size distribution but also the effective surface area of the reactive minerals, we utilize the effective-surface-area ratio, ω, which has a value between zero and one. A convenient choice for modeling the distribution of a variable bounded by zero and one is the beta distribution. The probability density function of the beta distribution is

$$p(\omega) = \frac{\Gamma(a+b)\omega^{a-1}(1-\omega)^{b-1}}{\Gamma(a)\Gamma(b)}, \tag{28}$$

where $\Gamma(\cdot)$ is the gamma function. Variables a and b shape the beta distribution.

The specific surface area over porosity, S/ϕ, which is a part of the Darcy-scale Damköhler number, equations (16) and (17), can be defined as

$$\frac{S}{\phi} = \frac{2\sum_{i=1}^{N}\omega_i r_i}{\sum_{i=1}^{N}(r_i)^2} = \frac{2\mathrm{E}(\omega r)}{\mathrm{E}(r^2)}. \tag{29}$$

Such a definition of S/ϕ depends on the pore geometry. Inferring from Hussaini and Dvorkin (2021)'s compilation of specific surface area versus porosity using digital images of natural rocks, S/ϕ can range from 0.15 (Fontainebleau sandstone) to 0.7 (Kentucky sandstone) when $\mathrm{E}(\omega) = 1$.

2.4 A constitutive relation for reaction at the Darcy scale

A constitutive relation is an additional equation that specifies properties of a material. For example, the longitudinal dispersivity describes the dispersion of solute introduced by variations in fluid velocities in a porous material. In this section, we develop a constitutive relation that models the average solute concentration of a porous medium with varying reaction rates in pores.

2.4.1 First-order kinetics

Before we approach the full reactive transport problems – equations (6) and (23) – we start with a single pore involving only mineral dissolution,

$$\frac{dC}{dt} = Da(1 - C), \quad C(t = 0) = C_0, \tag{30}$$

where C_0 is the initial concentration of the mineral-forming solute in the pore. We consider an aspect ratio, r/L_z, small enough such that a volume-averaged concentration is representative. Using equation (10), the Damköhler number in a cylindrical pore is

$$Da = \frac{2\omega}{r}\frac{L_z^2 k_\mathrm{p}}{D}, \tag{31}$$

where $2\omega/r$ defines the pore-scale geometry and $L_z^2 k_\mathrm{p}/D$ defines the physics of the problem. In this work, we focus on analyzing how pore-scale geometry affects solute concentration and reaction rate over time and assume $L_z^2 k_\mathrm{p}/D$ constant. We abbreviate $L_z^2 k_\mathrm{p}/D$ to Da_p. The solution for the single-pore reaction problem is

$$C(t;\, \omega, r) = (C_0 - 1)e^{(-2\, Da_\mathrm{p}\, \omega/r)t} + 1. \tag{32}$$

We define the volume-averaged solution as

$$C_\mathrm{avg}(t) = \frac{\displaystyle\int_0^1 \int_0^\infty C(t;\, \omega, r)p(\omega, r)r^2 dr d\omega}{\displaystyle\int_0^\infty p(r)r^2 dr} \tag{33}$$

$$= (C_0 - 1)\frac{\displaystyle\int_0^1 \int_0^\infty e^{(-2\, Da_\mathrm{p}\, \omega/r)t} p(\omega, r)r^2 dr d\omega}{\displaystyle\int_0^\infty p(r)r^2 dr} + 1. \tag{34}$$

The bounds of the integral over the pore size, r, should correspond to the bounds of the prescribed pore-size distribution. Consider $C_0 = 0$ and expand the volume-averaged solution using a Taylor series around $t = 0$:

$$C_\mathrm{avg}(t) = -\sum_{k=0}^{\infty}\left(\frac{1}{k!}\int_0^1\int_0^\infty \left(\frac{-2\, Da_\mathrm{p}\, \omega t}{r}\right)^k p(\omega, r)r^2 dr d\omega\right)/\mathrm{E}(r^2) + 1 \tag{35}$$

$$= -\sum_{k=1}^{\infty}\left(\frac{(-2\, Da_\mathrm{p}\, t)^k}{k!}\int_0^1\int_0^\infty p(\omega, r)\omega^k r^{2-k} dr d\omega\right)/\mathrm{E}(r^2) \tag{36}$$

$$= -\sum_{k=1}^{\infty}\left(\frac{(-2\, Da_\mathrm{p}\, t)^k}{k!}\frac{\mathrm{E}(\omega^k r^{2-k})}{\mathrm{E}(r^2)}\right) \tag{37}$$

$$= 2\, Da_\mathrm{p}\, t\frac{\mathrm{E}(\omega r)}{\mathrm{E}(r^2)} - 2(Da_\mathrm{p}\, t)^2\frac{\mathrm{E}(\omega^2)}{\mathrm{E}(r^2)} + O(t^3). \tag{38}$$

Let us now describe the Darcy-scale reaction in the same manner as we did for a single pore, equation (30). In this case, the definition of the Darcy-scale Damköhler number,

$$Da_{\mathrm{d}} = 2\, Da_{\mathrm{p}}\, \frac{\mathrm{E}(\omega r)}{\mathrm{E}(r^2)}, \tag{39}$$

leads to a first-order approximation of the volume-averaged concentration. To better approximate C_{avg}, we propose a nonlinear reaction-rate model as a constitutive relation,

$$\frac{d\overline{C}}{dt} = Da_{\mathrm{d}}(1-\overline{C})^n, \quad \overline{C}(t=0) = C_0, \tag{40}$$

where n is the reaction order (Lasaga, 1998). Many researchers have attempted to explain values for the reaction order in terms of dissolution or precipitation processes (e.g., Blum & Lasaga, 1987; Teng et al., 2000). However, attributions of a process on the basis of the value of this exponent is generally not defensible without further observations (Brantley, 2008). For further discussion, see Brantley (2003, 2008).

The solution to the nonlinear reaction-rate model, equation (40), is

$$\overline{C}(t) = 1 - \left[Da_{\mathrm{d}}(n-1)\, t + (1-C_0)^{1-n}\right]^{1/(1-n)}. \tag{41}$$

Its Taylor series expansion around $t=0$ while $C_0 = 0$ is

$$\overline{C}(t) = 1 - \sum_{k=0}^{\infty} \frac{\prod_{j=1}^{k-1}\left(j(n-1)+1\right)}{k!}(-\,Da_{\mathrm{d}}\, t)^k \tag{42}$$

$$= Da_{\mathrm{d}}\, t - \frac{n}{2}(Da_{\mathrm{d}}\, t)^2 + \frac{n(2n-1)}{6}(Da_{\mathrm{d}}\, t)^3 + O(t^4). \tag{43}$$

We observe that the Darcy-scale Damköhler number, equation (39), still matches the first-order term of the volume-averaged solution, equation (38). If we define

$$n = \frac{\mathrm{E}(\omega^2)\mathrm{E}(r^2)}{\mathrm{E}^2(\omega r)}, \tag{44}$$

then the nonlinear reaction-rate model approximates the volume-averaged concentration to the second order with respect to time. By Cauchy-Schwarz inequality, we infer $n \geq 1$, which agrees with experimental observations. The inverse square root of this definition of the reaction order, n, is also known as Tucker's congruence coefficient, which assesses similarity between two variables (Lorenzo-Seva & ten Berge, 2006).

Figure 1 shows scatter plots of pore sizes and effective-surface-area ratios. Each point represents an observation of the pore size and the effective-surface-area ratio in a porous sample. Tucker's congruence coefficient, r_c, measures the similarity between pore size and effective-surface-area ratio. From the leftmost figure to the rightmost figure, the congruence coefficient decreases as the observations become less similar, or more heterogeneous. Since the reaction order, n, is the squared inverse of the congruence coefficient, the reaction order increases as the heterogeneity increases. Such a definition of the reaction order is a function of the geometric variables ω and r. Thus we can use the reaction order to infer pore-scale spatial heterogeneity of minerals.

2.4.2 Second-order kinetics

We model the single-pore problem with second-order kinetics by

$$\frac{dC}{dt} = Da(1-C^2), \quad C(t=0) = 0, \tag{45}$$

where the solution is

$$C = \tanh\left(Da \cdot t\right), \tag{46}$$

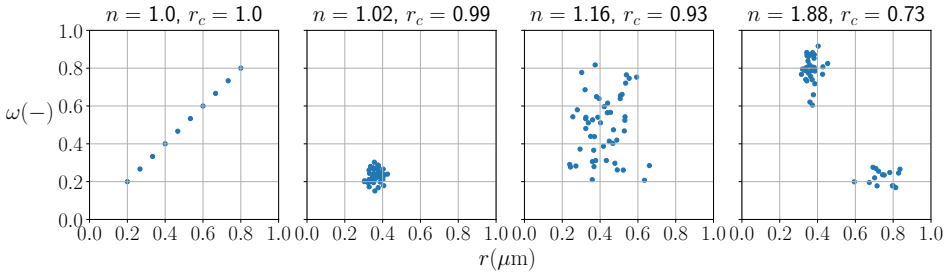

Figure 1. This figure shows scatter plots of pore sizes and effective-surface-area ratio. The title of each plot shows the reaction order, n, and Tucker's congruence coefficient, r_c.

which is an odd function. Using equation (7), the Damköhler number in a cylindrical pore is

$$Da = \frac{2\omega}{r}\frac{L_z^2\sqrt{k_d k_p}}{D}, \tag{47}$$

where $L_z^2\sqrt{k_\mathrm{d}k_\mathrm{p}}/D$, which we abbreviate to Da_p, defines the physics of the problem for second-order kinetics. The volume-averaged concentration is defined using equation (33), and we apply a Taylor series expansion to the volume-averaged concentration,

$$C_\mathrm{avg}(t) = \sum_{k=1}^{\infty}\left(\frac{B_{2k}4^k(4^k-1)}{(2k)!}\int_0^1\int_0^\infty\left(\frac{2\,Da_\mathrm{p}\,\omega t}{r}\right)^{2k-1}p(\omega,r)r^2 dr d\omega\right)/\mathrm{E}(r^2) \tag{48}$$

$$= \sum_{k=1}^{\infty}\left(\frac{B_{2k}4^k(4^k-1)(2\,Da_\mathrm{p}\,t)^{2k-1}}{(2k)!}\int_0^1\int_0^\infty p(\omega,r)\omega^{2k-1}r^{3-2k}dr d\omega\right)/\mathrm{E}(r^2) \tag{49}$$

$$= 2\,Da_\mathrm{p}\,t\frac{\mathrm{E}(\omega r)}{\mathrm{E}(r^2)} - \frac{(2\,Da_\mathrm{p}\,t)^3}{3}\frac{\mathrm{E}(\omega^3 r^{-1})}{\mathrm{E}(r^2)} + O((Da_\mathrm{p}\,t)^5), \tag{50}$$

where B_{2k} is the Bernoulli number (Oldham et al., 2009). The Taylor series expansion of the hyperbolic tangent function, equation (46), converges for $Da\,t < \pi/2$, which is not of concern since we utilize only the derivatives of $C_\mathrm{avg}(t=0)$.

We propose the following constitutive relation that describes the solute concentration at the Darcy scale,

$$\frac{d\overline{C}}{dt} = Da_\mathrm{d}(1-\overline{C}^2)^n, \quad \overline{C}(t=0) = 0. \tag{51}$$

We do not attempt to find a solution for $\overline{C}$. However, we can still expand $\overline{C}$ around $t = 0$ with a Taylor series:

$$\overline{C} = Da_\mathrm{d}\,t - \frac{n(n+1)}{6}(Da_\mathrm{d}\,t)^3 + O(t^4), \tag{52}$$

which is also an odd function. See Appendix B for detailed derivations. Comparing the third-order term of equation (50) with that of equation (52) yields

$$\frac{n(n+1)}{2} = \frac{\mathrm{E}(\omega^3 r^{-1})\mathrm{E}^2(r^2)}{\mathrm{E}^3(\omega r)}. \tag{53}$$

One can utilize the quadratic formula to explicitly determine n,

$$n = \left(-1 + \sqrt{1 + 8\mathrm{E}(\omega^3 r^{-1})\mathrm{E}^2(r^2)/\mathrm{E}^3(\omega r)}\right)/2, \tag{54}$$

where we consider only the larger value of n as a solution. Note that the reaction orders for first- and second-order kinetics are non-dimensional and, most importantly, independent of the length scale and the reaction rate constants.

2.5 Goodness of fit between the pore-scale and the Darcy-scale concentrations

There exists a variety of goodness-of-fit measures between models and experimental observations. For example, the coefficient of determination, R^2, is often used to determine the kinetic rate law when applying the integral method (Brantley & Conrad, 2008; Zhao & Skelton, 2014). The mean-squared error is also a goodness-of-fit measure, and the least-squares approach tends to minimize such a metric. We use another goodness-of-fit measure, the Jensen-Shannon divergence, which is based on the Kullback-Leibler divergence (Kullback & Leibler, 1951). The Kullback-Leibler divergence between some unknown distribution, $p(x)$, and an approximating distribution, $q(x)$, is:

$$\mathrm{KL}(p\|q) = \int p(x) \log_2 \left(\frac{p(x)}{q(x)} \right) dx. \tag{55}$$

The Kullback-Leibler divergence satisifies $\mathrm{KL}(p\|q) \geq 0$ with equality if, and only if, $p(x) = q(x)$ (Bishop, 2006). Although $\mathrm{KL}(p\|q) \geq 0$, it may diverge to infinity depending on the underlying densities (F. Nielsen, 2020). Thus we use the Jensen-Shannon divergence,

$$\begin{aligned} \mathrm{JS}(p\|q) =& \frac{1}{2} \left(\mathrm{KL} \left(p \| \frac{p+q}{2} \right) + \mathrm{KL} \left(q \| \frac{p+q}{2} \right) \right) & (56) \\ =& \frac{1}{2} \int \left(p(x) \log_2 \left(\frac{2p(x)}{p(x)+q(x)} \right) + q(x) \log_2 \left(\frac{2q(x)}{p(x)+q(x)} \right) \right) dx, & (57) \end{aligned}$$

which is bounded between 0 and 1 when using base-2 logarithms (Lin, 1991). Throughout this work, we use the Jensen-Shannon distance, which is defined as the square root of the Jensen-Shannon divergence.

Such a metric measures the distance between probability distributions (Endres & Schindelin, 2003; Österreicher & Vajda, 2003; Levene & Kononovicius, 2019). The following describes how we apply this measure to solute concentration over time, $C_{\mathrm{avg}}(t)$ and $\overline{C}(t)$. Suppose we regard solute concentration over time as cumulative distribution functions. In that case, we measure the Jensen-Shannon divergence of their derivatives, which can be seen as the probability density functions or the reaction rates over time.

When the observed solute concentration is not monotonically increasing over time like a cumulative distribution function, we simply use the root-mean-square error (RMSE) as a quality measure of the constitutive relation,

$$\mathrm{RMSE} = \sqrt{\frac{\int (p(x) - q(x))^2 dx}{\max(x) - \min(x)}}. \tag{58}$$

2.6 Determination of the Darcy-scale Damköhler number, Da_{d}, and the reaction order, n, using power series

We test the constitutive relation using the volume-averaged concentration, $C_{\mathrm{avg}}(t)$, which is an analogy of solute concentration measurements from a dissolution experiment. Assume the solute concentration can be described by the constitutive relation within a certain error. Then we can use the Taylor series expansions, equations (43) and (52), to obtain the Darcy-scale Damköhler number,

$$Da_{\mathrm{d}} = C'_{\mathrm{avg}}(t = 0), \tag{59}$$

which is the initial rate of reaction. When the kinetics is of first order, the reaction order is obtained by differentiating equation (43) twice,

$$n = -\frac{C''_{\mathrm{avg}}(t=0)}{(Da_{\mathrm{d}})^2}. \tag{60}$$

Differentiating equation (52) thrice and rearranging yields the reaction order for second-order kinetics,

$$n(n+1) = -\frac{C'''_{\mathrm{avg}}(t=0)}{(Da_{\mathrm{d}})^3}. \tag{61}$$

This method of determining Da_{d} and n utilizes power-series expansion and requires only the derivatives of the solute concentration at $t = 0$.

We consider three sets of log-normally distributed pore sizes, R_1, R_2, and R_3, which have $S/\phi \approx 0.6$ but different variances. The pore sizes are chosen such that they range from 10–80 μm (Gong et al., 2020). Likewise, we assume the effective surface area follows the beta distribution, where Ω_1 considers most pores fully reactive, Ω_2 assumes a larger variance of mineral surface area in the pores, and Ω_3 implies that the reactive mineral constitutes a small portion of the porous sample. Figure 2 shows the details of the aforementioned probability distributions.

The products of the random variables R and Ω form nine scenarios of the bundle-of-tubes model, which can be used as benchmarks for our power-series approach to obtain the Darcy-scale Damköhler number and the reaction order. We compare this method with a goodness-of-fit minimization using both Da_{d} and n as unknowns, similar to the ideas of nonlinear least-squares model fitting (Fogler, 2016). Initially, the pores are filled with dissolving fluid with no solute concentration, $C = 0$. Then the mineral starts to dissolve into the fluid, such that the solute concentration increases. We assume we can observe the average concentration, C_{avg}, without transport effects. To capture the full reaction behavior, the simulation ends when the solute concentration, C_{avg}, is larger than 0.99. The physics related parameters, Da_{p}, is set as 50, such that the Darcy-scale Damköhler numbers of the scenarios are at a similar scale.

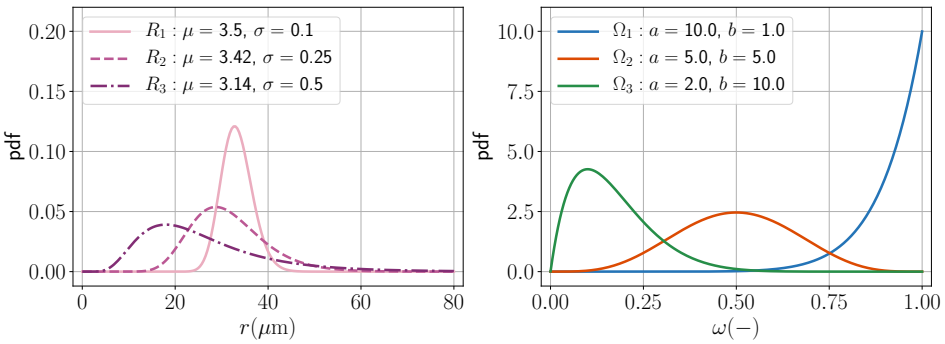

Figure 2. This figure shows the probability density functions of the distribution of pore sizes and effective-surface-area ratio. The legends state the essential parameters for generating the probability density functions.

2.7 Flow-through experiment

In the previous section, we test the constitutive relation considering only mineral reaction. To measure the solute concentration of the fluid in a porous sample, one has

to push the fluid out of the porous sample. We now discuss this full reactive transport problem. Consider a flow-through experiment, i.e., injecting fluid that dissolves the mineral in a porous sample. We collect the fluid from the outlet and measure the solute concentration over time. Before the experiment, the porous sample should be saturated by the dissolving fluid. After a certain amount of time, the fluid has accumulated an initial solute concentration. Then we start the flow-through experiment by injecting fluid without solute under high Péclet number. We take fluid samples from the outlet and measure the solute concentration. Since we are injecting fluid with zero solute concentration, we expect the measured solute concentration at the outlet to decrease over time. When the outlet concentration is close to zero, we reduce the Péclet number to 0.1–1% of the original Péclet number in order to observe an increase of the outlet solute concentration. This process creates a V-shaped curve of outlet concentration over time.

We use FEniCS (Alnaes et al., 2015) to solve the transient initial boundary value problem of each pore and apply equation (33) to obtain the average concentration. Details of the numerical methods are explained in Appendix C. We assume the porous sample can be described by a combination of the pore-size distribution, R_1, and the effective-surface-area ratio, Ω_3. In the following subsections, we discuss two cases of low and high Damköhler numbers. In both cases, we consider the molecular diffusivity, D, as $5 \times 10^{-9}\,\mathrm{m^2\,s^{-1}}$.

2.7.1 The low Damköhler-number case, $Da_\mathrm{d} = 0.1$

The Darcy-scale Damköhler number, equation (39), is proportional to the length scale squared. This case is suitable when the mineral has low reaction rates or when the porous domain is short (small length scale), e.g., a 5 cm rock sample in a laboratory. We consider this our "small length-scale scenario" for which the outlet solute concentration can be measured. Since the Damköhler number is low, the solute concentration during injection of the dissolving fluid should be far from chemical equilibrium. Therefore, we assume the reaction is of first order.

Following the procedure of the flow-through experiment, we set the initial Péclet number as 10 and the Darcy-scale Damköhler number is 0.1. We reduce the Péclet number to 0.01 at 0.15 nondimensional time. The simulation ends at 1.5 nondimensional time, which for the 5 cm rock sample mentioned above would correspond to about 8.7 days.

The solute concentration over time at the outlet of the porous sample is collected from the simulation data. Knowing the Péclet number and that the mineral reaction is of first order, we fit the observed concentration over time with the reactive transport model,

$$\frac{\partial \overline{C}}{\partial t} + Pe_\mathrm{d}\,\frac{\partial \overline{C}}{\partial z} - \left(1 + (Pe_\mathrm{d})^2 t\, f(r)\right) \frac{\partial^2 \overline{C}}{\partial z^2} = Da_\mathrm{d}(1-\overline{C})^n. \tag{62}$$

The shape factor, $f(r)$, is defined using equation (21). Utilizing the optimization procedures in SciPy (Virtanen et al., 2020), we find Da_d and n by minimizing the RMSE between the observation and the model.

Another method of fitting Da_d and n is to utilize a part of $C_\mathrm{avg}(t)$, where the diffusion effects are dominant enough ($Pe \ll 1$) such that we can treat the concentration as constant over space. Owing to the divergence theorem and the boundary condition $C(0,t) = 0$, results in

$$\frac{\partial \overline{C}}{\partial t} + Pe_\mathrm{d}\,\overline{C}(1,t) = Da_\mathrm{d}(1-\overline{C})^n. \tag{63}$$

Then, we can perform least-squares fitting on the left-hand side to determine Da_{d} and n. Figure 3 shows the outlet concentration of the flow-through experiment and highlights the region in which we consider diffusion to be dominant. Such an approach relies heavily on the strong-diffusion assumption, and is therefore not suitable for the high Damköhler-number case, discussed in the next section.

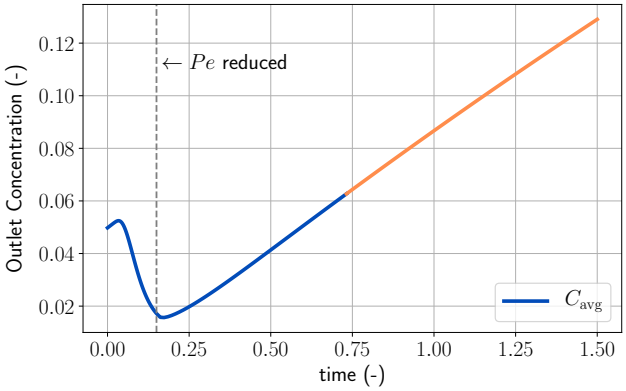

Figure 3. The outlet concentration over time of the low Damköhler-number problem. The orange line shows the part, where we apply the least-squares fitting technique (equation (63)). The vertical dashed line indicates the time, $t = 0.15$, when the injection rate is reduced.

2.7.2 The high Damköhler-number case, $Da_{\mathrm{d}} = 4 \times 10^4$

Consider a field experiment in an aquifer, where the length scale is on the order of meters. Here, a fluid is injected in one well and produced at another well. In this case, it may not be possible to observe a concentration breakthrough at the outlet. Thus, we perform simulations of a flow-through experiment and measure the solute concentration at the inlet over time. The Darcy-scale Damköhler number is 4×10^4. We assume a second-order kinetics model for the mineral reaction, and our reactive transport model is

$$\frac{\partial \overline{C}}{\partial t} + Pe_{\mathrm{d}} \frac{\partial \overline{C}}{\partial z} - \left(1 + (Pe_{\mathrm{d}})^2 t\, f(r)\right) \frac{\partial^2 \overline{C}}{\partial z^2} = Da_{\mathrm{d}}(1 - \overline{C}^2)^n. \tag{64}$$

We consider three cases of intial Péclet numbers, 4×10^3, 8×10^3, and 8×10^4. The injection stops at 2×10^{-6} dimensionless time, and the simulation ends at 1×10^{-5} dimensionless time, which is roughly 231.5 days considering a 100 m simulation domain.

Though it is practically not possible to observe the inlet concentration during the injection phase, we perform the fitting of Da_{d}, n, and $f(r)$ using all information of C_{avg} at the inlet. In the latter phase when injection stops (rising limb of the curve in Figure 3), it should be possible to determine the concentration at the inlet by sampling the fluid in the injection well.

3 Results

In this section, we show the benchmarks of the power-series approach and the simulations of flow-through experiments. Then, we discuss the results in section 4.

3.1 Benchmark of the power-series approach

We benchmark the power-series approach that obtains the reaction order, n, and the Darcy-scale Damköhler number, Da_{d}, using a bundle of tubes characterized by the distributions of pore sizes and effective-surface-area ratio described in Section 2.6.

Figures 4 and 5 show the benchmark for the first-order kinetics and the second-order kinetics, respectively. In the upper part of the figures, we plot the contour lines of log-scaled Jensen Shannon divergence between C_{avg} and $\overline{C}$. The red points indicate the approximation of Da_{d} and n using the power-series approach. In an ideal case, the red points should be in the minimum of the Jensen Shannon divergence. In the lower part of the figures, we plot the concentration over time of the scenarios that performed the worst.

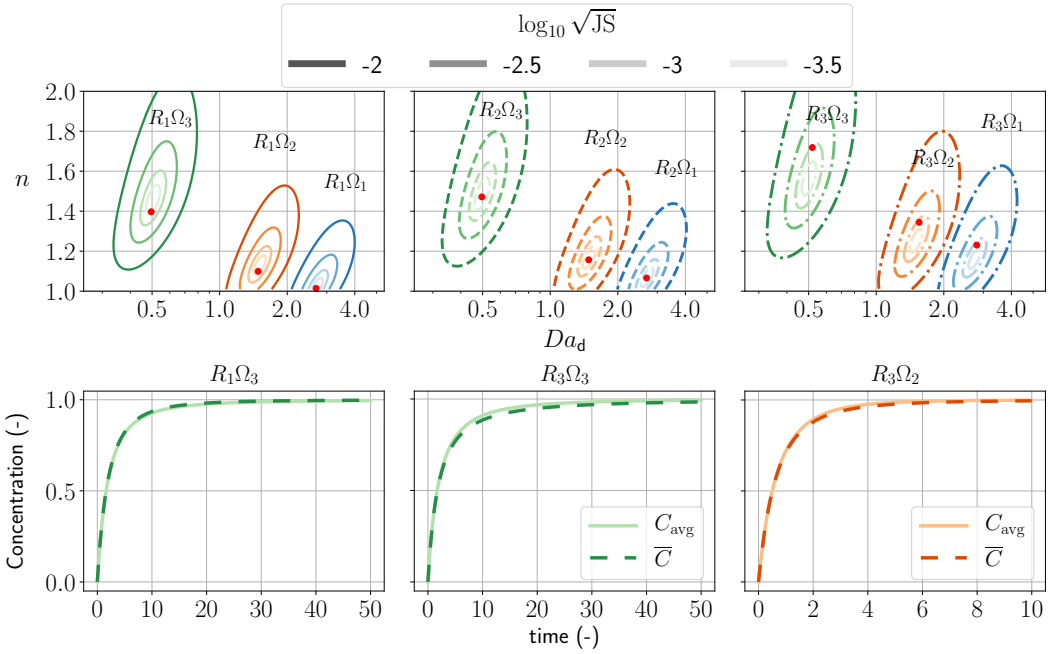

Figure 4. The upper part of the figure shows the contours of the log-scaled Jensen Shannon divergence between the observed concentration and the modeled concentration of first-order kinetics using the constitutive relation. The red points are the Darcy-scale Damköhler number and the reaction order approximated by the power-series approach (equations (59) and (60)). The legend shows the value of the log-scaled Jenson Shannon divergence using a gray scale, corresponding to the brightness of the colored contour lines. The lower part of the figure shows the concentrations over time C_{avg} and $\overline{C}$ of the scenarios $R_1\Omega_3$, $R_3\Omega_3$, and $R_3\Omega_2$.

3.2 Flow-through experiment

Figure 6 shows the observed concentration, C_{avg}, and the modeled concentration, $\overline{C}$. Table 1 shows the Darcy-scale Damköhler number, the reaction order, and shape factor obtained by direct calculation (equations (39), (44) and (54)) and by RMSE minimization of the low and high Damköhler-number cases ($Da_{\mathrm{d}} = 0.1$ and $Da_{\mathrm{d}} = 40\,000$, respectively) and corresponding to the $R_1\Omega_3$ distribution. The results of the least-squares curve fitting method, used only in the low Damköhler-number scenario, are $Da_{\mathrm{d}} = 0.1$ and $n = 1.38$.

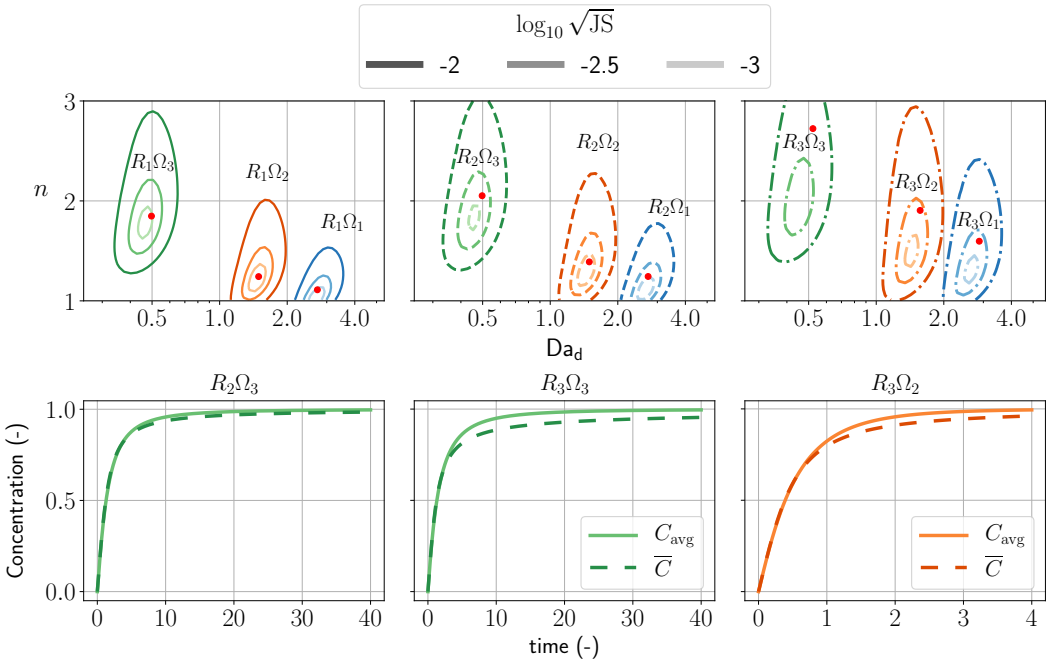

Figure 5. The upper part of the figure shows the contours of the log-scaled Jensen Shannon divergence between the observed concentration and the modeled concentration of second-order kinetics using the constitutive relation. The red points are the Darcy-scale Damköhler number and the reaction order approximated by the power series approach (equations (59) and (61)). The legend shows the value of the log-scaled Jenson Shannon divergence using a gray scale, corresponding to the brightness of the colored contour lines. The lower part of the figure shows the concentrations over time C_avg and $\overline{C}$ of the scenarios $R_2\Omega_3$, $R_3\Omega_3$, and $R_3\Omega_2$, respectively.

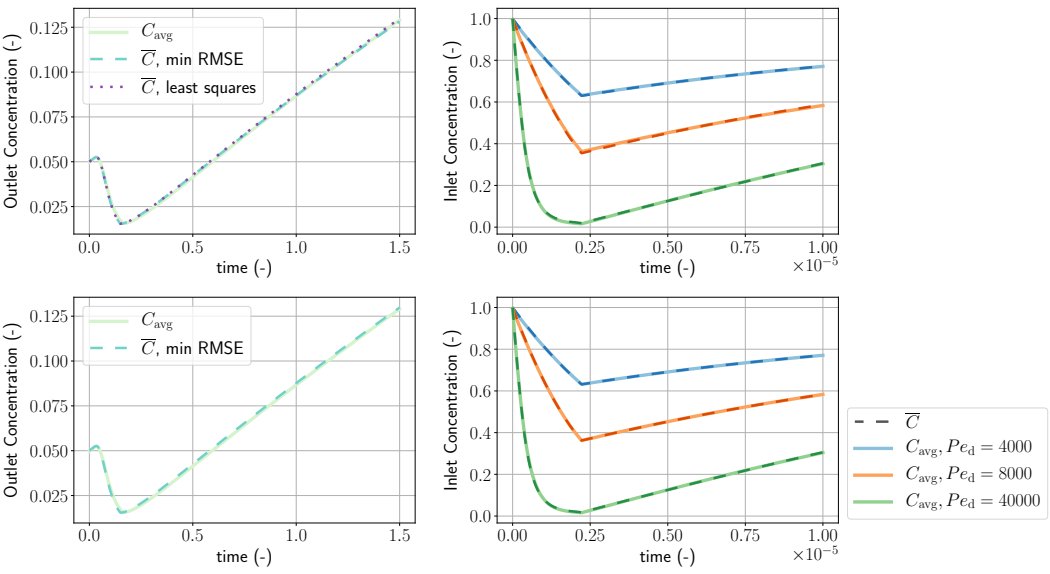

Figure 6. The figures show the concentration C_avg (solid lines) and the modeled concentration $\overline{C}$ (dashed lines) of the low and high Damköhler-number cases on the left and right panels, respectively. The top panel shows the cases with fitting Da_d and n. The bottom panel shows the cases with fitting Da_d, n, and the shape factor, $f(r)$, additionally.

Table 1. This table summarizes the Darcy-scale Damköhler number, Da_{d}, the reaction order, n, and the shape factor, $f(r)$, obtained by fitting the concentration-over-time curve using the constitutive relation with the RMSE metric. The values of the direct calculation are the result of prescribing Da_{p} and the $R_1\Omega_3$ distribution. In the low Da_{d} case, we assumed first-order kinetics. Hence we use equation (44) to calculate the reaction order. We assumed second-order kinetics for the high Da case, and equation (54) is used for calculating the reaction order for second-order kinetics.

Initial Pe_{d}	10	4 000	8 000	40 000
	Direct calculation			
Da_{d}	0.1	40 000		
n	1.40	1.77		
$f(r)$	4.081×10^{-2}			
	Minimum RMSE			
Da_{d}	0.1	52 528	45 154	38 464
n	1.57	1.57	1.66	1.30
	Minimum RMSE with shape factor fitting			
Da_{d}	0.1	50 887	42 049	38 950
n	1.68	1.55	1.59	1.53
$f(r)$	2.39×10^{-2}	1.402×10^{-1}	1.222×10^{-1}	3.168×10^{-2}

4 Discussion

4.1 Benchmark of the power-series approach

In Figure 4, we observed that the power-series approach obtains Da_{d} and n close to the minimum Jensen Shannon distance. The connections between nonlinear fitting of the parameters, Da_{d} and n, and the geometric information of the porous medium are established since the power-series approach is exact for retrieving expected values of the pore-size and the effective-surface-area distributions.

In Figure 5, we observed general agreement of Da_{d} and n obtained by the power-series approach to those at the minimum Jensen Shannon distance. As the variance of the pore-size increases, the obtained Da_{d} and n (red points) stray from the minimum Jensen Shannon distance. In the selected concentration plots, the modeled concentration fits well when $\overline{C} < 0.5$. Some discrepancy between $\overline{C}$ and C_{avg} is present when $\overline{C} > 0.5$. Comparing to the results of first-order kinetics, where $\overline{C}$ fits C_{avg} well throughout all concentrations, our averaged model of second-order kinetics can only fit reactions far from equilibrium (e.g., $\overline{C} < 0.5$).

The power-series approach of obtaining Da_{d} and n suffers from the fact that:

1. reaction rates at zero concentration can be hard to obtain, and
2. numerical differentiation of higher-order derivatives can yield spurious results.

Therefore, we require other nonlinear fitting methods by minimizing the divergence between models and observations. In the next section, we discuss the intricacies of nonlinear fitting of solute concentration during flow-through experiments.

4.2 Flow-through experiment

The top-left panel of Figure 6 shows the low Damköhler-number, first-order-reaction case, where both the RMSE minimization and the least-squares fitting method fits the outlet concentration, C_{avg}. Both methods of obtaining Da_{d} and n are accurate within 15% relative error as confirmed by direct calculation from pore-size and effective-surface-area distributions. The good agreement can be attributed to the fact that the solute can be mostly flushed out from the porous domain, due to the low Damköhler number. Hence, the solute concentration in each tube goes down to almost zero, and spatial gradients of the solute concentration in the z direction are negligible. This creates a situation similar to the problem considering only reaction effects, which is not the case for the scenarios of high Damköhler-number, second-order kinetics.

Focusing on the high Damköhler-number scenarios, we observe general agreement of fitted parameters. For the case of initial $Pe_{\text{d}} = 4\,000$, the error in Da_{d} can be attributed to the fact that the volume injected is not enough, such that the dissolution in smaller pores is not observed in C_{avg}. The case of initial $Pe_{\text{d}} = 8\,000$ approximated Da_{d} closer to the prescribed value than the previous case. The third case of initial $Pe_{\text{d}} = 40\,000$, performed the best in retrieving Da_{d}. This may be because this case is similar to the low Damköhler-number case, in which the initial solute concentration of all pores is pushed out from the porous domain, such that C_{avg} is close to zero. The purpose of comparing these three cases is to emphasize that the inversion of parameters is influenced by how we perform the injection test, namely, by the selection of the initial Péclet number.

Furthermore, we performed a fitting in all cases considering the shape factor as unknown. The bottom panels of Figure 6 show the cases where we fit the shape factor, $f(r)$, in addition to Da_{d} and n. For the low Damköhler number case, we have a good fit of $f(r)$ within an order of magnitude. However, the obtained value for n exhibits a bigger error. This signals the vagueness of the reaction order and the shape factor in minimizing RMSE, where increasing or decreasing either one of the variables leads to similar RMSE.

For the high Damköhler number cases, the obtained Da_{d} improved slightly comparing to the cases with a prescribed shape factor. All fitted shape factors are within an order of magnitude compared to the theoretical calculations. In particular, for the case of initial $Pe_{\text{d}} = 40\,000$, we observe a good fit of the retrieved shape factor. Although imperfect, our method of parameter estimation using a solute concentration breakthrough curve is useful for modeling the average behavior of reactive transport in porous media. The results suggest that it is possible to infer pore-scale information using the inversion of averaged parameters.

Figure 7 shows the concentration in pores, the averaged concentration, and the modeled concentration of the high Damköhler number, initial $Pe_{\text{d}} = 40\,000$ scenario. When the injection stops, the increase of the inlet solute concentration is not only due to the reaction, but also due to the diffusion of solute from the reservoir to the inlet. We attribute the underestimated n to our reactive transport model, equation (64), not being able to capture the diffusion effects in each pore, which results in a lower reaction order. Certainly, this situation is not as ideal as the low Damköhler-number situation. Though, the modeled concentration, $\overline{C}$, still represents the average behavior of the pore concentrations.

In all of the flow-through experiments, we considered only one observation point, either the fluid inlet or the fluid outlet. This work serves as a demonstration of the base case with only one observation. To improve the fitting of the reaction order of the high Damköhler-number cases, one can incorporate more observation points, spatially distributed within the domain.

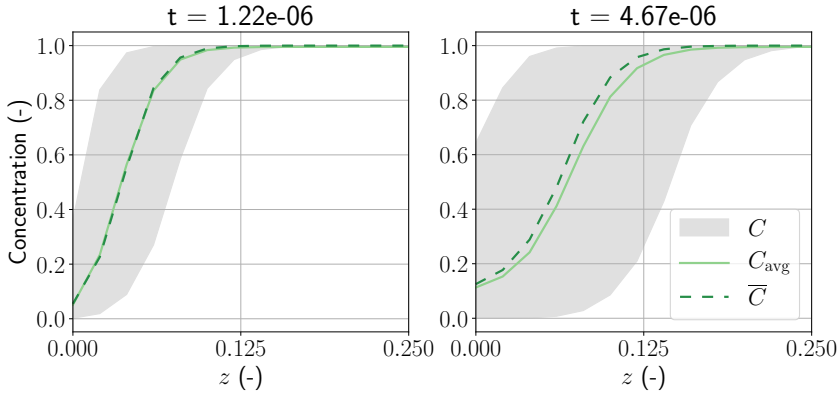

Figure 7. This figure shows the solute concentration in the pores, C, the averaged concentration, C_{avg}, and the modeled concentration, $\overline{C}$, of the initial $Pe_{\mathrm{d}} = 40\,000$ scenario without shape factor fitting. The left panel shows the solute concentration in the porous domain during fluid injection. The right panel shows the solute concentration after fluid injection has stopped, as indicated by the increasing fluid inlet concentration.

4.3 The applicability of the constitutive relations

By adding an exponent to the pore-scale reaction model, the Darcy-scale reaction model effectively describes the averaged behavior of reactions taking place independently in different pores of the porous medium. We examine the applicability of the simple approach using the averaged concentration of first-order kinetics as an example. The averaged concentration, equation (34), can be considered as a continuous mixture of exponential distributions,

$$C_{\mathrm{avg}}(t) = 1 - \int_0^\infty e^{-\lambda t} p(\lambda) d\lambda, \tag{65}$$

where λ is a parameter that characterizes the exponential distributions. The finite mixture is known as the hyperexponential distribution, which is utilized for fitting long-tail distributions (Feldmann & Whitt, 1998; Okada et al., 2020). If λ is a gamma distribution, then $C_{\mathrm{avg}}(t)$ is a Pareto distribution (Balakrishna & Lai, 2009). The concentration of our proposed model, equation (41), has the following form when $C_0 = 0$:

$$\overline{C}(t) = 1 - \left[1 + Da_{\mathrm{d}}(n-1)\, t\right]^{1/(1-n)}, \tag{66}$$

which is the cumulative distribution function of the Pareto distribution, also called the Lomax distribution. There exists a particular ratio distribution of the effective surface area and the pore sizes, Ω/R, that satisfies $\overline{C} = C_{\mathrm{avg}}$. Such an existence contributes to the effectiveness of the constitutive relation for the first-order kinetics.

In contrast, the theoretical basis of constitutive relations for second-order kinetics is less distinct. We simply followed the derivations of first-order kinetics and exploited the oddity of C_{avg} and $\overline{C}$ to obtain a second-order approximation. The solution for second-order kinetics in a single pore, equation (46), can be recast to

$$C = \tanh\left(Da \cdot t\right) = \frac{1 - e^{-2\,Da\,\cdot t}}{1 + e^{-2\,Da\,\cdot t}}, \tag{67}$$

which is a cumulative distribution function of a scaled logistic distribution. If we consider time a semi-infinite domain $[0, \infty)$, such a distribution is also known as the half

logistic distribution (Balakrishnan, 1985). Though we did not find or derive the relationships of the logistic distribution mixture, we denote the possibility of approximating such a mixture using the Pareto distribution, equation (66), since the hyperbolic tangent function can be represented by a Laurent series,

$$\tanh(t) = 1 - 2\sum_{k=0}^{\infty}(-1)^k e^{-2t(k+1)},\ t > 0, \tag{68}$$

which is a mixture of exponential distributions. Such expansion techniques would avoid relying on derivatives around $C = 0$ as is done in this study, which may be advantageous but requires more research.

4.4 Limitations and outlook

The main limitation of this study is that the reaction model we considered is simple and may not be adequate to describe complex geochemical processes, e.g., a rock sample which consists of multiple dissolving minerals. Though we considered two common models of first- and second-order kinetics, we treat the rate constant, k_d and k_p, as constant and, indeed, k_d and k_p may change as temperature, pH, or ionic strength changes.

Moreover, the assumption that chemical reactions in each tube occur independently of the other tubes is idealized. In pore-network modeling, the porous medium is discretized as a network of pore bodies and pore throats, and the coordination number is defined as number of connections to each pore body. Experimental studies have reported that the average coordination number of a sandstone is ~ 4 (e.g., Ioannidis & Chatzis, 2000; Øren & Bakke, 2003; Hefny et al., 2020). Our bundle-of-tubes model has an average coordination number of 0 (or 1, if one considers the pores reside at the fluid inlet and outlet boundaries), which is the base case for pore-network modeling. For this base case, the reaction order does not depend on Pe_{d} or Da_{d}. The dependence of the reaction order on Pe_{d} or Da_{d} for larger coordination numbers requires further studies.

Nonetheless, our simple model reveals a possible mechanistic explanation to the usage of the Darcy-scale reaction order larger than one, and how it can reveal geometric information of the porous medium using the solute breakthrough curve. We suggest considerations of the aforementioned limitations as potential topics for future research.

We propose another possible application of this work in view of energy conservation in a porous sample, where there is only one definition of temperature of the fluid, T_{f}^*, and the porous solid, T_{s}^*. A special case of energy conservation without pressure work and viscous heating is analogous to equation (1):

$$\frac{\partial T_{\mathrm{f}}^*}{\partial t^*} + u\frac{\partial T_{\mathrm{f}}^*}{\partial z^*} - D_{\mathrm{f}}\frac{\partial^2 T_{\mathrm{f}}^*}{\partial z^{*2}} = q_T, \tag{69}$$

where D_{f} is the thermal diffusivity of the fluid and q_T is a heat source introduced by the porous solid. Usually, such an energy conservation model of heat tracer tests assumes thermal equilibrium between the fluid and the porous solid, $T_{\mathrm{f}} = T_{\mathrm{s}}$, (Shook, 2001; Anderson, 2005; Saar, 2011). However, studies and modeling on thermal disequilibrium between fluid and solid phases have gained interest lately (Karani & Huber, 2017; Koch et al., 2021). If we consider a heat tracer test, where we create a breakthrough curve like the ones in Figure 3, we can model the behavior by

$$\frac{\partial T_{\mathrm{f}}^*}{\partial t^*} + u\frac{\partial T_{\mathrm{f}}^*}{\partial z^*} - D_{\mathrm{f}}\frac{\partial^2 T_{\mathrm{f}}^*}{\partial z^{*2}} = \frac{\overline{D}A}{V_{\mathrm{f}}}\frac{(T_{\mathrm{s}}^* - T_{\mathrm{f}}^*)}{L^*}, \tag{70}$$

where $\overline{D}$ is a certain average of the thermal diffusivity of the porous medium, and L^* is a characteristic length that defines the heat flux between the solid-fluid boundary.

The formulation is similar to our study of reactive transport with first-order kinetics. Therefore, it is possible to apply the same techniques described in this work to obtain the "reaction order" and infer pore-scale information.

5 Conclusion

Mineral reaction kinetics defined at the pore scale are not necessarily valid at the Darcy scale. We utilize a bundle-of-tubes model to study the modeling of dissolution kinetics in porous media at the Darcy scale. By adding an exponent, n (i.e. the Darcy-scale reaction order), to first- and second-order kinetics, the resulting constitutive relation approximates the average dissolution rate of the bundle-of-tubes model. Using the pore-size and the effective-surface-area ratio distributions to characterize the tube bundles, we expand the solute concentration of dissolving species with Taylor series and thus relate the Darcy-scale Damköhler number, Da_{d}, and reaction order with the distribution moments. The Taylor-series expansions show that the Darcy-scale reaction order of first-order kinetics is the inverse square root of Tucker's congruence coefficient (also known as the cosine similarity) between the pore sizes and effective-surface-area ratios. Therefore, an increase of reaction order indicates an increase of pore-scale heterogeneity. Such a relation gives a mechanistic meaning to the reaction order.

Furthermore, we simulate flow-through experiments of dissolving porous media at the laboratory as well as the field scale and discuss how one can utilize the constitutive relation by fitting a solute concentration breakthrough curve with Da_{d} and n as unknowns. As an additional benefit, we discuss cases of the flow-through experiments where the shape factor of longitudinal dispersivity is also considered as a fitting parameter. The inversion is successful, and the fitted parameters are close to the prescribed parameters calculated by the moments of pore-size and effective-surface-area ratio distributions. We infer that:

1. detailed pore-scale information (characterized by functions of moments) can be inferred using averaged Darcy-scale quantities (such as solute concentration), and
2. by analyzing the solute concentration of dissolving minerals over time using flow-through experiments, we can acquire the Darcy-scale reaction order and the dispersion coefficient, which represent heterogeneity at the pore scale.

The relations we derived provide us a quantitative approach to measure the spatial heterogeneity of a porous domain using the Darcy-scale reaction order and reveal a mechanistic explanation for $n > 1$.

Appendix A Derivation of the longitudinal dispersivity using spatial moment analysis

We introduce an advection equation of solute concentration in a pore

$$\frac{\partial C^*}{\partial t^*} + u\frac{\partial C^*}{\partial z^*} = 0. \tag{A1}$$

The velocity, u, is defined using equation (12)

$$\frac{\partial C^*}{\partial t^*} + \frac{r^2}{8}\frac{\Delta P}{\mu L_z}\frac{\partial C^*}{\partial z^*} = 0. \tag{A2}$$

When injecting a solute pulse at $x = 0$, the center of mass of the solute is located at

$$z^*(t^*; r) = r^2\frac{\Delta P}{8\mu L_z}t^*. \tag{A3}$$

Similar to the volume averaging procedure, Eq. (33), we define the center of mass in a bundle of tubes system

$$\bar{z}^*(t^*) = \frac{\int_0^\infty z^*(t^*;r) r^2 p(r) dr}{\int_0^\infty r^2 p(r) dr} = \frac{\mathrm{E}(r^4)}{\mathrm{E}(r^2)} \frac{\Delta P}{8\mu L_z} t^*. \tag{A4}$$

Following the procedures of spatial moment analysis (Goltz & Roberts, 1987; Dentz & de Barros, 2013; Lee et al., 2018; Natarajan & Kumar, 2018), the mean velocity is

$$\bar{u} = \frac{d\bar{z}^*}{dt^*} = \frac{\mathrm{E}(r^4)}{\mathrm{E}(r^2)} \frac{\Delta P}{8\mu L_z} \tag{A5}$$

which is the volume averaged velocity, equation (18). The change of spatial variance over time is

$$\sigma_z^2 = \frac{\int_0^\infty (z^*(t^*;r))^2 r^2 p(r) dr}{\int_0^\infty r^2 p(r) dr} - (\bar{z}^*(t^*))^2 \tag{A6}$$

$$= \left(\frac{\mathrm{E}(r^6)}{\mathrm{E}(r^2)} - \frac{\mathrm{E}^2(r^4)}{\mathrm{E}^2(r^2)} \right) \left(\frac{\Delta P}{8\mu L_z} t^* \right)^2 \tag{A7}$$

$$= \left(\frac{\mathrm{E}(r^6)\mathrm{E}(r^2)}{\mathrm{E}^2(r^4)} - 1 \right) \left(\frac{\mathrm{E}(r^4)}{\mathrm{E}(r^2)} \frac{\Delta P}{8\mu L_z} t^* \right)^2 \tag{A8}$$

$$= \left(\frac{\mathrm{E}(r^6)\mathrm{E}(r^2)}{\mathrm{E}^2(r^4)} - 1 \right) (\bar{u} t^*)^2 \tag{A9}$$

The longitudinal dispersion coefficient is

$$D_\mathrm{L} = \frac{1}{2} \frac{d\sigma_z^2}{dt} = \left(\frac{\mathrm{E}(r^6)\mathrm{E}(r^2)}{\mathrm{E}^2(r^4)} - 1 \right) \bar{u}^2 t^*, \tag{A10}$$

which concludes the derivation of equation (21). The nondimensional solute transport equation is

$$\frac{\partial \overline{C}}{\partial t} + Pe_\mathrm{d} \frac{\partial \overline{C}}{\partial z} - \left(1 + (Pe_\mathrm{d})^2 t\, f(r)\right) \frac{\partial^2 \overline{C}}{\partial z^2} = 0. \tag{A11}$$

Following Crank (1975), the fundamental solution of the aforementioned transport equation is

$$\overline{C}(z,t) = \frac{1}{\sqrt{4\pi(t + (Pe_\mathrm{d}\, t)^2/2)}} \exp\left(-\frac{(z - z_0 - Pe_\mathrm{d}\, t)^2}{4(t + (Pe_\mathrm{d}\, t)^2/2)} \right). \tag{A12}$$

We test the validity of the dispersion coefficient by comparing with volume-averaged solute concentration, equation (7). We consider two cases of pore size distributions R_1 and R_2 with initial injection at $z_0 = 0$ and $Pe_\mathrm{d} = 10$.

Figure A1 shows the comparison between $\overline{C}$ and C_avg at different time steps. When the travel distance increases, the difference between $\overline{C}$ and C_avg increases. Such effect is more pronounced when σ is larger, as shown in the right panel of Figure A1. Higher order method of moments are employed for better modeling of dispersion effects (Chatwin, 1970; Zhang et al., 2008; Vikhansky & Ginzburg, 2014; Jiang & Chen, 2019). However, we limit our analysis to second order to focus on the topic of Darcy-scale reaction order.

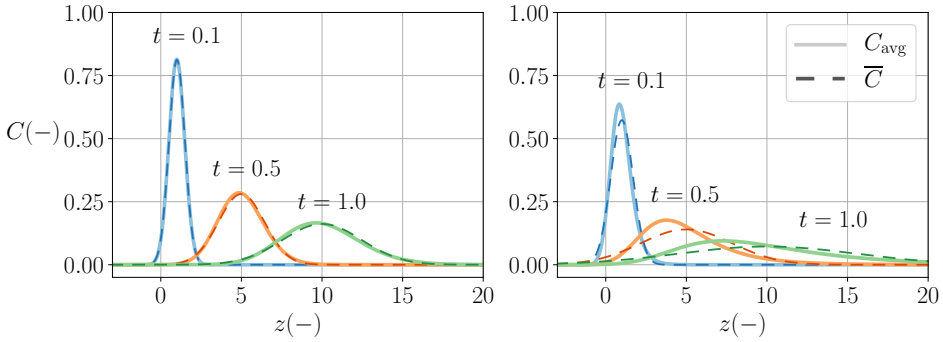

Figure A1. Comparison of the volume-averaged solute concentration and the modeled concentration. The left panel shows the case of pore size distribution R_1, and the right panel shows the case of pore size distribution R_2.

Appendix B Taylor series of the averaged second-order kinetics model

The averaged second-order kinetics model, equation (51), is

$$\overline{C}^{'} = Da_{\mathrm{d}} \left(1 - \overline{C}^2\right)^n. \tag{B1}$$

We show derivations of expanding equation (B1) using a Taylor series. A Taylor series expansion of $\overline{C}$ around $t = 0$ is

$$\overline{C}(t) = \overline{C}(0) + \overline{C}^{'}(0)t + \frac{\overline{C}^{''}(0)}{2}t^2 + \frac{\overline{C}^{'''}(0)}{6}t^3 + O(t^4), \tag{B2}$$

which consists of derivatives of $\overline{C}$. Differentiate equation (B1)

$$\overline{C}^{''} = -2\, Da_{\mathrm{d}}\, n \left(1 - \overline{C}^2\right)^{n-1} \overline{C}\, \overline{C}^{'}. \tag{B3}$$

The initial condition, $\overline{C}(0) = 0$, leads to $\overline{C}^{''}(0) = 0$, which corresponds to the second-order term in equation (50). Instead of performing further differentiation, we rearrange equation (B1)

$$\overline{C}^{'} = Da_{\mathrm{d}} \left(1 - \overline{C}\right)^n \left(1 + \overline{C}\right)^n. \tag{B4}$$

Applying the binomial approximation to $(1 + \overline{C})^n$ yields

$$\overline{C}^{'} \approx Da_{\mathrm{d}} \left(1 - \overline{C}\right)^n \left(1 + n\overline{C}\right) \text{ for } |n\overline{C}| \ll 1. \tag{B5}$$

Differentiate

$$\overline{C}^{''} = Da_{\mathrm{d}}\, n\overline{C}^{'} \left(-\left(1 - \overline{C}\right)^{n-1} \left(1 + n\overline{C}\right) + \left(1 - \overline{C}\right)^n\right), \tag{B6}$$

which retains the property $\overline{C}^{''}(0) = 0$. Further differentiate and omit $\overline{C}^{''}$

$$\overline{C}^{'''} = Da_{\mathrm{d}}\, n\overline{C}^{'} \Big((n-1)\left(1 - \overline{C}\right)^{n-2} \left(1 + n\overline{C}\right) \overline{C}^{'} \tag{B7}$$

$$- n\left(1 - \overline{C}\right)^{n-1} \overline{C}^{'} - n\left(1 - \overline{C}\right)^{n-1} \overline{C}^{'}\Big). \tag{B8}$$

Hence,

$$\overline{C}^{'''}(0) = -(Da_{\mathrm{d}})^3\, n(n+1). \tag{B9}$$

Therefore, the Taylor series with an approximated third-order derivative is

$$\overline{C}(t) = Da_{\mathrm{d}}\, t - \frac{n(n+1)}{6}(Da_{\mathrm{d}}\, t)^3 + O(t^4). \tag{B10}$$

Appendix C Numerical methods of the reactive transport model

The continuity equation of the concentration is

$$\frac{\partial C}{\partial t} + \nabla \cdot (f(C)) = q, \tag{C1}$$

where f is a function that defines the flux and q represents a source or sink of the concentration. The conservative form of the continuity equation is

$$\int_\Omega \frac{\partial C}{\partial t} d\Omega + \int_{\partial\Omega} f(C) \cdot \mathbf{n} ds = \int_\Omega q d\Omega, \tag{C2}$$

where Ω is an arbitrary control volume, $\partial\Omega$ denotes the boundary of the control volume, and $\mathbf{n}$ is the outward normal vector of the control volume. Following Koren (1993), a cell-centered finite volume discretization of equation (C2) in one dimension is

$$\int_{\Omega_j} \frac{\partial C}{\partial t} dz + f(C)\Big|_{j+1/2} - f(C)\Big|_{j-1/2} = \int_{\Omega_j} q dz, \tag{C3}$$

where the half-integer indices $j-1/2$ and $j+1/2$ refer to the cell faces $\partial\Omega_{j-1/2}$ and $\partial\Omega_{j+1/2}$, as illustrated in Figure C1. Instead of approximating the fluxes with a first-order upwind scheme, we utilize the κ interpolation scheme, originated from van Leer (1985),

$$f_{j+1/2} = f_j + \frac{1+\kappa}{4}(f_{j+1} - f_j) + \frac{1-\kappa}{4}(f_j - f_{j-1}),\ \kappa \in [-1, 1]. \tag{C4}$$

The flux term $f(C)|_{j+1/2}$ is abbreviated as $f_{j+1/2}$. We use a second-order upwind scheme, $\kappa = -1$, for linear advection $f(C) = C$ such that

$$f_{j+1/2} = C_j + \frac{1}{2}(C_j - C_{j-1}). \tag{C5}$$

Consider a Total Variation Diminishing (TVD) framework (Sweby, 1984), we define the ratio of concentration gradient assuming constant mesh size

$$r_{j+1/2} = \frac{f'(C)|_{j+1/2}}{f'(C)|_{j-1/2}} = \frac{C_{j+1} - C_j}{C_j - C_{j-1}}. \tag{C6}$$

A flux limiter is a function that selects spatial discretization schemes based on the ratio of concentration gradient. In the case of linear advection, we apply the flux limiter $\psi(r)$ to equation (C5)

$$f_{j+1/2} = C_j + \frac{\psi(r)}{2}(C_j - C_{j-1}). \tag{C7}$$

When $\psi(r) = 1$, we have the second-order upwind flux, and when $\psi(r) = r$, a centered difference flux is recovered. Note that the flux reduces to first-order given $\psi(r) = 0$. We choose the minmod limiter (Roe, 1986)

$$\psi(r) = \max(0, \min(1, r)), \tag{C8}$$

which switches the advection flux between second-order upwind and centered difference in the second-order TVD region. Following the Discontinous Galerkin approach (Rivière, 2008), we reformulate the reactive transport model in a single pore, equation (6),

$$\int_\Omega v \frac{\partial C}{\partial t} d\Omega + \int_{\partial\Omega} v \left(Pe\, C - \frac{\partial C}{\partial z} \right) \cdot \mathbf{n} ds = \int_\Omega v\, Da(1 - C) d\Omega, \tag{C9}$$

where v is a piecewise constant test function. We calculate the diffusion flux using the two-point flux approximation. Closely following the derivations of Roy et al. (2019) and utilize the flux-limited advection, we have

$$\int_\Omega v\frac{\partial C}{\partial t}d\Omega + \int_{\Gamma_{\text{int}}}[v]\left(\text{adv}(C)\,Pe\cdot\mathbf{n} + \frac{[C]}{h}\right)dS = \int_\Omega v\,Da(1-C)d\Omega, \tag{C10}$$

$$\text{adv}(C) = C^{\text{up}} + \frac{\psi(r)}{2}\left(C^{\text{up}} - C^{\text{upup}}\right), \tag{C11}$$

where Γ_{int} denote the union of all interior boundaries, h is the distance between two cell centers, and $[\cdot]$ is the jump operator. The superscript "up" denotes the upwind cell, and "upup" represents the upwind cell of the aforementioned upwind cell. For example, when the surface integral is performed over $\partial\Omega_{j+1/2}$, the advection term is

$$\text{adv}(C)\Big|_{j+1/2} = C_j + \frac{\psi(r)}{2}(C_j - C_{j-1}), \tag{C12}$$

which is the advection flux, equation (C7). Before we define the temporal discretization scheme, we abbreviate equation (C10)

$$\int_\Omega v\frac{\partial C}{\partial t}d\Omega = -\int_{\Gamma_{\text{int}}}[v]\text{adv}(C)\,Pe\cdot\mathbf{n}dS - F^{\text{D}}(C) + F^{\text{q}}(C), \tag{C13}$$

where $F^{\text{D}}(C)$ is the diffusion term, and $F^{\text{q}}(C)$ represents the reaction term. To approach second order accuracy in time, we utilize the explicit midpoint method

$$\int_\Omega v\frac{C^{n+1/2}-C^n}{0.5\Delta t}d\Omega = -\int_{\Gamma_{\text{int}}}[v]C^{\text{up},n}\,Pe\cdot\mathbf{n}dS - F^{\text{D}}(C^n) + F^{\text{q}}(C^n), \tag{C14}$$

$$\int_\Omega v\frac{C^{n+1}-C^n}{\Delta t}d\Omega = -\int_{\Gamma_{\text{int}}}[v]\text{adv}(C^{n+1/2})\,Pe\cdot\mathbf{n}dS - F^{\text{D}}(C^{n+1/2}) + F^{\text{q}}(C^{n+1/2}), \tag{C15}$$

where Δt is the time step size. The superscripts n, $n+1/2$, and $n+1$ refers to current time step, midpoint step, and the next time step, respectively. The midpoint value $C^{n+1/2}$ is approximated using first-order upwind advection. Then we apply the flux limiter to the second step. To ensure numerical stability, the explicit midpoint method should follow the time step size limitation proposed by (Prabhakaran & Jones Tarcius Doss, 2015)

$$\Delta t \le \frac{h^2}{2 + Pe\,h}. \tag{C16}$$

Although the time step size limitation is derived for flux-limited advection diffusion equations with no source terms, it is treated as a maximum value for the time step size in the simulations while using the explicit midpoint method. The time step size limitation restricts the efficiency of explicit methods. Rearrange equation (C16)

$$\frac{Pe\,\Delta t}{h} \le 1 - \frac{2\Delta t}{h^2}, \tag{C17}$$

where $Pe\,\Delta t/h$ is the CFL number, and $2\Delta t/h^2$ is the Fourier number. The maximum CFL number allowed while using the explicit upwind scheme is 1 normally. However, the explicit centered difference treatment of diffusion causes a degradation of the maximum CFL number in equation (C17). To alleviate this issue, one may consider an implicit time discretization scheme for diffusion. This idea leads to the implicit-explicit (IMEX) time-discretization scheme, which consists of applying an implicit discretization for diffusion and an explicit one for advection (Ascher et al., 1997; Pareschi &

673 Russo, 2005; Boscarino et al., 2015). Of many possible implementations of IMEX
674 schemes, we implement the following

$$\int_\Omega v \frac{C^{n+1/2} - C^n}{0.5\Delta t} d\Omega = -\int_{\Gamma_{\text{int}}} [v] C^{\text{up},n}\, Pe \cdot \mathbf{n} dS - F^{\text{D}}(C^{n+1/2}) + F^{\text{q}}(C^n), \tag{C18}$$

$$\int_\Omega v \frac{C^{n+1} - C^n}{\Delta t} d\Omega = -\int_{\Gamma_{\text{int}}} [v] \text{adv}(C^{n+1/2})\, Pe \cdot \mathbf{n} dS - \frac{1}{2} F^{\text{D}}(C^{n+1/2}) - \frac{1}{2} F^{\text{D}}(C^{n+1}) + F^{\text{q}}(C^{n+1/2}), \tag{C19}$$

675 where both steps include implicit diffusion terms. We benchmark the numerical
676 method based on the solution of tracer transport with first order decay

$$C(z,t) = 1 - \frac{M}{\sqrt{4\pi(t+t_0)}} \exp\left(-\frac{(z - z_0 - Pe\, t)^2}{4(t+t_0)} - Da\, t\right), \tag{C20}$$

677 where z_0 is the center of mass of the inverted Gaussian, M and t_0 are the parameters
678 adjusted to bound the initial concentration between 0 and 1. In the benchmark, we
679 set the initial condition with $M = 0.2$, $t_0 = 5 \times 10^{-3}$, and $z_0 = 0.5$. The mesh
680 size, h, is 0.04. For the explicit midpoint scheme, the time step size is 5×10^{-4}, and
681 for the IMEX scheme, the time step size is 5×10^{-3}. The simulation ends at 0.1
682 nondimensional time.

683 Figure C2 and C3 shows the benchmark result at different time steps, and both
684 numerical solution agrees with the analytical solution. However, since the IMEX
685 scheme allows larger time step size during simulations, we use only the IMEX scheme
686 in our simulations.

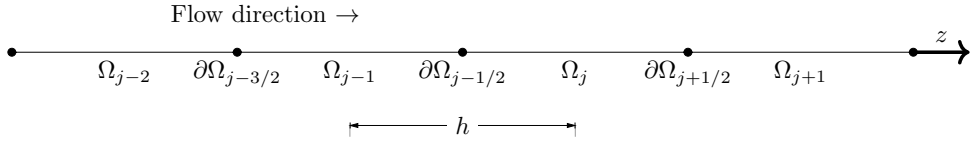

Figure C1. An illustration of the cell-centered finite volume grid.

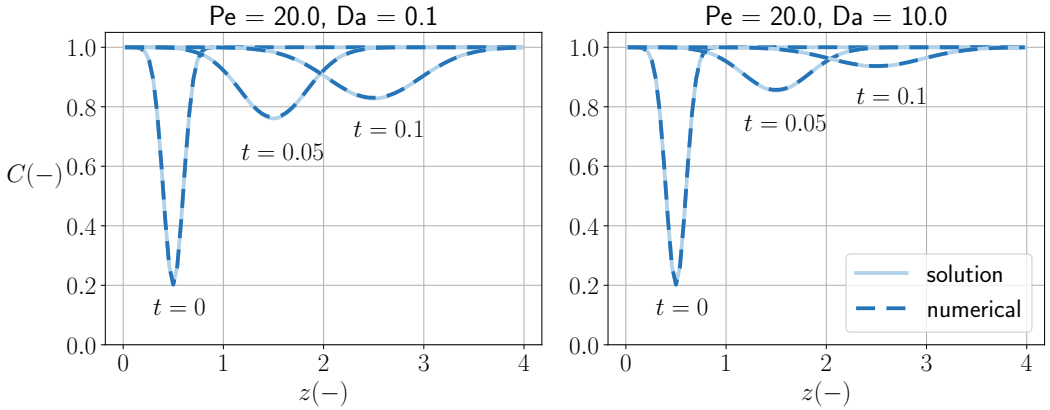

Figure C2. Benchmark of the numerical methods with analytical solutions of tracer transport with first-order decay using the explicit midpoint scheme. The CFL number is 0.25.

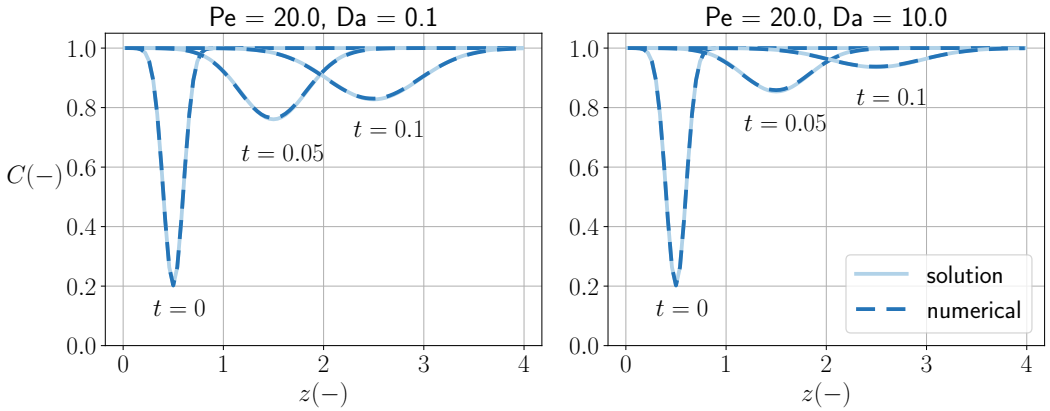

Figure C3. Benchmark of the numerical methods with analytical solutions of tracer transport with first order decay using the IMEX scheme. The CFL number is 2.5.

Acknowledgments

This work is supported by the Swiss National Science Foundation project, entitled "Analysing spatial scaling effects in mineral reaction rates in porous media with a hybrid numerical model". We also thank the Werner Siemens-Stiftung (Werner Siemens Foundation) for its support of the Geothermal Energy and Geofluids (GEG.ethz.ch) Group at ETH Zurich, Switzerland.

References

Al-Khulaifi, Y., Lin, Q., Blunt, M. J., & Bijeljic, B. (2017). Reaction rates in chemically heterogeneous rock: Coupled impact of structure and flow properties studied by X-ray microtomography. *Environmental Science Technology*, *51*, 4108–4116. https://doi.org/10.1021/acs.est.6b06224

Al-Khulaifi, Y., Lin, Q., Blunt, M. J., & Bijeljic, B. (2018). Reservoir-condition pore-scale imaging of dolomite reaction with supercritical CO_2 acidified brine: Effect of pore-structure on reaction rate using velocity distribution analysis. *International Journal of Greenhouse Gas Control*, *68*, 99–111. https://doi.org/10.1016/j.ijggc.2017.11.011

Al-Khulaifi, Y., Lin, Q., Blunt, M. J., & Bijeljic, B. (2019). Pore-scale dissolution by CO_2 saturated brine in a multimineral carbonate at reservoir conditions: Impact of physical and chemical heterogeneity. *Water Resources Research*, *55*, 3171–3193. https://doi.org/10.1029/2018WR024137

Alnaes, M. S., Blechta, J., Hake, J., Johansson, A., Kehlet, B., Logg, A., ... Wells, G. N. (2015). The FEniCS project version 1.5. *Archive of Numerical Software*, *3*, 9–23. 10.11588/ans.2015.100.20553

Anderson, M. P. (2005). Heat as a ground water tracer. *Groundwater*, *43*(6), 951–968. https://doi.org/10.1111/j.1745-6584.2005.00052.x

Arriaza, J. L., & Ghezzehei, T. A. (2013). Explaining longitudinal hydrodynamic dispersion using variance of pore size distribution. *Journal of Porous Media*, *16*, 11–19. https://doi.org/10.1615/JPorMedia.v16.i1.20

Ascher, U. M., Ruuth, S. J., & Spiteri, R. J. (1997). Implicit-explicit Runge-Kutta methods for time-dependent partial differential equations. *Applied Numerical Mathematics*, *25*(2), 151–167. (Special Issue on Time Integration) https://doi.org/10.1016/S0168-9274(97)00056-1

Balakrishna, N., & Lai, C. D. (2009). Univariate distributions. In *Continuous bivariate distributions: Second edition* (pp. 1–32). New York, NY: Springer New

York. https://doi.org/10.1007/b101765_1

Balakrishnan, N. (1985). Order statistics from the half logistic distribution. *Journal of Statistical Computation and Simulation*, *20*(4), 287–309. https://doi.org/10.1080/00949658508810784

Bishop, C. (2006). *Pattern recognition and machine learning*. Springer-Verlag New York.

Blum, A. E., & Lasaga, A. C. (1987). Monte Carlo simulations of surface reaction rate laws. In W. Stumm (Ed.), *Aquatic surface chemistry: Chemical processes at the particle-water interface* (pp. 255–292). Wiley.

Boscarino, S., Bürger, R., Mulet, P., Russo, G., & Villada, L. M. (2015). Linearly implicit IMEX Runge-Kutta methods for a class of degenerate convection-diffusion problems. *SIAM Journal on Scientific Computing*, *37*(2), B305–B331. https://doi.org/10.1137/140967544

Brantley, S. L. (2003). Reaction kinetics of primary rock-forming minerals under ambient conditions. In H. D. Holland & K. K. Turekian (Eds.), *Treatise on geochemistry* (pp. 73–117). Oxford: Pergamon. https://doi.org/10.1016/B0-08-043751-6/05075-1

Brantley, S. L. (2008). Kinetics of mineral dissolution. In S. L. Brantley, J. D. Kubicki, & A. F. White (Eds.), *Kinetics of water-rock interaction* (pp. 151–210). Springer, New York, NY.

Brantley, S. L., & Conrad, C. F. (2008). Analysis of rates of geochemical reactions. In S. L. Brantley, J. D. Kubicki, & A. F. White (Eds.), *Kinetics of water-rock interaction* (pp. 1–38). Springer, New York, NY.

Buscheck, T. A., Bielicki, J. M., Chen, M., Sun, Y., Hao, Y., Edmunds, T. A., ... Randolph, J. B. (2014). Integrating CO_2 storage with geothermal resources for dispatchable renewable electricity. *Energy Procedia*, *63*, 7619–7630. (12th International Conference on Greenhouse Gas Control Technologies, GHGT-12) https://doi.org/10.1016/j.egypro.2014.11.796

Carbonell, R. G. (1979). Effect of pore distribution and flow segregation on dispersion in porous media. *Chemical Engineering Science*, *34*, 1031–1039. https://doi.org/10.1016/0009-2509(79)80003-2

Chatwin, P. C. (1970). The approach to normality of the concentration distribution of a solute in a solvent flowing along a straight pipe. *Journal of Fluid Mechanics*, *43*(2), 321–352. https://doi.org/10.1017/S0022112070002409

Crank, J. (1975). Concentration-dependent diffusion: Methods of solution. In *The mathematics of diffusion* (2nd ed., pp. 104–136). Oxford University Press.

Cussler, E. L. (2009). Homogeneous chemical reactions. In *Diffusion: Mass transfer in fluid systems* (3rd ed., p. 478—512). Cambridge University Press. https://doi.org/10.1017/CBO9780511805134.019

Dentz, M., & de Barros, F. P. J. (2013). Dispersion variance for transport in heterogeneous porous media. *Water Resources Research*, *49*(6), 3443–3461. https://doi.org/10.1002/wrcr.20288

Ebigbo, A., Phillips, A., Gerlach, R., Helmig, R., Cunningham, A. B., Class, H., & Spangler, L. H. (2012). Darcy-scale modeling of microbially induced carbonate mineral precipitation in sand columns. *Water Resources Research*, *48*(7). https://doi.org/10.1029/2011WR011714

Endres, D. M., & Schindelin, J. E. (2003). A new metric for probability distributions. *IEEE Transactions on Information Theory*, *49*, 1858–1860. https://doi.org/10.1109/TIT.2003.813506

Feldmann, A., & Whitt, W. (1998). Fitting mixtures of exponentials to long-tail distributions to analyze network performance models. *Performance Evaluation*, *31*(3), 245–279. https://doi.org/10.1016/S0166-5316(97)00003-5

Fischer, C., Kurganskaya, I., Schäfer, T., & Lüttge, A. (2014). Variability of crystal surface reactivity: What do we know? *Applied Geochemistry*, *43*, 132–157. https://doi.org/10.1016/j.apgeochem.2014.02.002

Fischer, C., & Luttge, A. (2017). Beyond the conventional understanding of water–rock reactivity. *Earth and Planetary Science Letters*, *457*, 100–105. https://doi.org/10.1016/j.epsl.2016.10.019

Fogler, H. S. (2016). *Elements of chemical reaction engineering.* Prentice Hall.

Goltz, M. N., & Roberts, P. V. (1987). Using the method of moments to analyze three-dimensional diffusion-limited solute transport from temporal and spatial perspectives. *Water Resources Research*, *23*(8), 1575–1585. https://doi.org/10.1029/WR023i008p01575

Gong, L., Nie, L., & Xu, Y. (2020). Geometrical and topological analysis of pore space in sandstones based on X-ray computed tomography. *Energies*, *13*, 3774. https://doi.org/10.3390/en13153774

Hefny, M., Qin, C., Saar, M. O., & Ebigbo, A. (2020). Synchroton-based pore-network modeling of two-phase flow in nubian sandstone and implications for capillary trapping of carbon dioxide. *International Journal of Greenhouse Gas Control*, *103*, 103164. https://doi.org/10.1016/j.ijggc.2020.103164

Hussaini, S. R., & Dvorkin, J. (2021). Specific surface area versus porosity from digital images. *Journal of Petroleum Science and Engineering*, *196*, 107773. https://doi.org/10.1016/j.petrol.2020.107773

Ioannidis, M., & Chatzis, I. (2000). On the geometry and topology of 3d stochastic porous media. *Journal of Colloid and Interface Science*, *229*(2), 323–334. https://doi.org/10.1006/jcis.2000.7055

Jiang, W., & Chen, G. (2019). Environmental dispersion in layered wetland: Moment based asymptotic analysis. *Journal of Hydrology*, *569*, 252–264. https://doi.org/10.1016/j.jhydrol.2018.12.005

Jung, H., & Navarre-Sitchler, A. (2018a). Physical heterogeneity control on effective mineral dissolution rates. *Geochimica et Cosmochimica Acta*, *227*, 246–263. https://doi.org/10.1016/j.gca.2018.02.028

Jung, H., & Navarre-Sitchler, A. (2018b). Scale effect on the time dependence of mineral dissolution rates in physically heterogeneous porous media. *Geochimica et Cosmochimica Acta*, *234*, 70–83. https://doi.org/10.1016/j.gca.2018.05.009

Karani, H., & Huber, C. (2017). Role of thermal disequilibrium on natural convection in porous media: Insights from pore-scale study. *Physical Review E*, *95*, 033123. https://doi.org/10.1103/PhysRevE.95.033123

Kaufmann, G., & Dreybrodt, W. (2007). Calcite dissolution kinetics in the system $CaCO_3$–H_2O–CO_2 at high undersaturation. *Geochimica et Cosmochimica Acta*, *71*(6), 1398–1410. https://doi.org/10.1016/j.gca.2006.10.024

Koch, T., Weishaupt, K., Müller, J., Weigand, B., & Helmig, R. (2021). A (dual) network model for heat transfer in porous media. *Transport in Porous Media*. https://doi.org/10.1007/s11242-021-01602-5

Koren, B. (1993). A robust upwind discretization method for advection, diffusion and source terms. In C. Vreugdenhil & B. Koren (Eds.), *Numerical methods for advection-diffusion problems* (pp. 117–138). Germany: Vieweg.

Kozeny, J. (1927). Über kapillare leitung des wassers im boden. *Wien Akad. Wiss.*, *136*, 271.

Kullback, S., & Leibler, R. A. (1951). On information and sufficiency. *Annals of Mathematical Statistics*, *22*, 79–86. https://doi.org/10.1214/aoms/1177729694

Lasaga, A. C. (1998). *Kinetic theory in the earth sciences.* Princeton University Press.

Lee, J., Rolle, M., & Kitanidis, P. K. (2018). Longitudinal dispersion coefficients for numerical modeling of groundwater solute transport in heterogeneous formations. *Journal of Contaminant Hydrology*, *212*, 41–54. (Advances in Experimental Techniques, Validation of Modelling Tools and Uncertainty in Predictions from Pore to Field Scale) https://doi.org/10.1016/

j.jconhyd.2017.09.004

Levene, M., & Kononovicius, A. (2019). Empirical survival Jensen-Shannon divergence as a goodness-of-fit measure for maximum likelihood estimation and curve fitting. *Communications in Statistics - Simulation and Computation*. https://doi.org/10.1080/03610918.2019.1630435

Levenson, Y., & Emmanuel, S. (2013). Pore-scale heterogeneous reaction rates on a dissolving limestone surface. *Geochimica et Cosmochimica Acta*, *119*, 188–197. https://doi.org/10.1016/j.gca.2013.05.024

Li, L., Peters, C. A., & Celia, M. A. (2007). Effects of mineral spatial distribution on reaction rates in porous media. *Water Resources Research*, *43*, W01419. https://doi.org/10.1029/2005WR004848

Li, L., & Salehikhoo, F. (2015). The role of magnesite spatial distribution patterns in determining dissolution rates: When do they matter? *Geochimica et Cosmochimica Acta*, *155*, 107–121. https://doi.org/10.1016/j.gca.2015.01.035

Li, L., Salehikhoo, F., & Brantley, S. L. (2013). Magnesite dissolution rates at different spatial scales: The role of mineral spatial distribution and flow velocity. *Geochimica et Cosmochimica Acta*, *108*, 91–106. https://doi.org/10.1016/j.gca.2013.01.010

Li, L., Salehikhoo, F., Brantley, S. L., & Heidari, P. (2014). Spatial zonation limits magnesite dissolution in porous media. *Geochimica et Cosmochimica Acta*, *126*, 555–573. https://doi.org/10.1016/j.gca.2013.10.051

Li, R., Yang, C., Ke, D., & Liu, C. (2020). The scaling of mineral dissolution rates under complex flow conditions. *Geochimica et Cosmochimica Acta*, *274*, 63–78. https://doi.org/10.1016/j.gca.2020.01.048

Lin, J. (1991). Divergence measures based on the shannon entropy. *IEEE Transactions on Information Theory*, *37*, 145–151. https://doi.org/10.1109/18.61115

Lorenzo-Seva, U., & ten Berge, J. M. F. (2006). Tucker's congruence coefficient as a meaningful index of factor similarity. *Methodology*, *2*, 57–64. https://doi.org/10.1027/1614-1881.2.2.57

Ma, J., Ahkami, M., Saar, M. O., & Kong, X.-Z. (2021). Quantification of mineral accessible surface area and flow-dependent fluid-mineral reactivity at the pore scale. *Chemical Geology*, *563*, 120042. https://doi.org/10.1016/j.chemgeo.2020.120042

Maher, K. (2010). The dependence of chemical weathering rates on fluid residence time. *Earth and Planetary Science Letters*, *294*, 101–110. https://doi.org/10.1016/j.epsl.2010.03.010

Mahmoodlu, M. G., Raoof, A., Bultreys, T., Van Stappen, J., & Cnudde, V. (2020). Large-scale pore network and continuum simulations of solute longitudinal dispersivity of a saturated sand column. *Advances in Water Resources*, *144*, 103713. https://doi.org/10.1016/j.advwatres.2020.103713

Meile, C., & Tuncay, K. (2006). Scale dependence of reaction rates in porous media. *Advances in Water Resources*, *29*(1), 62–71. https://doi.org/10.1016/j.advwatres.2005.05.007

Meng, X., & Yang, D. (2017). Dynamic Dispersion Coefficient of Solutes Flowing in a Circular Tube and a Tube-Bundle Model. *Journal of Energy Resources Technology*, *140*(1). (012903) https://doi.org/10.1115/1.4037374

Menke, H. P., Andrew, M. G., Blunt, M. J., & Bijeljic, B. (2016). Reservoir condition imaging of reactive transport in heterogeneous carbonates using fast synchrotron tomography - effect of initial pore structure and flow conditions. *Chemical Geology*, *428*, 15–26. https://doi.org/10.1016/j.chemgeo.2016.02.0300009-2541

Menke, H. P., Reynolds, C. A., Andrew, M. G., Pereira Nunes, J. P., Bijeljic, B., & Blunt, M. J. (2018). 4d multi-scale imaging of reactive flow in carbonates: Assessing the impact of heterogeneity on dissolution regimes using streamlines at multiple length scales. *Chemical Geology*, *481*, 27–37.

https://doi.org/10.1016/j.chemgeo.2018.01.016

Moore, J., Lichtner, P. C., White, A. F., & Brantley, S. L. (2012). Using a reactive transport model to elucidate differences between laboratory and field dissolution rates in regolith. *Geochimica et Cosmochimica Acta*, *93*, 235–361. https://doi.org/10.1016/j.gca.2012.03.021

Nancollas, G. H. (1968). Kinetics of crystal growth from solution. *Journal of Crystal Growth*, *3-4*, 335–339. https://doi.org/10.1016/0022-0248(68)90170-X

Natarajan, N., & Kumar, G. S. (2018). Spatial moment analysis of multispecies contaminant transport in porous media. *Environmental Engineering Research*, *23*(1), 76–83. https://doi.org/10.4491/eer.2016.147

Navarre-Sitchler, A., & Brantley, S. (2007). Basalt weathering across scales. *Earth and Planetary Science Letters*, *261*, 321–334. https://doi.org/10.1016/j.epsl.2007.07.010

Naviaux, J. D., Subhas, A. V., Rollins, N. E., Dong, S., Berelson, W. M., & Adkins, J. F. (2019). Temperature dependence of calcite dissolution kinetics in seawater. *Geochimica et Cosmochimica Acta*, *246*, 363–384. https://doi.org/10.1016/j.gca.2018.11.037

Nielsen, A. E. (1984). Electrolyte crystal growth mechanisms. *Journal of Crystal Growth*, *67*(2), 289–310. https://doi.org/10.1016/0022-0248(84)90189-1

Nielsen, F. (2020). On a generalization of the jensen-shannon divergence and the jensen-shannon centroid. *Entropy*, *22*, 221. https://doi.org/10.3390/e22020221

Noiriel, C., Steefel, C. I., Yang, L., & Ajo-Franklin, J. (2012). Upscaling calcium carbonate precipitation rates from pore to continuum scale. *Chemical Geology*, *318–319*, 60–74. https://doi.org/10.1016/j.chemgeo.2012.05.014

Okada, M., Yamanishi, K., & Masuda, N. (2020). Long-tailed distributions of inter-event times as mixtures of exponential distributions. *Royal Society Open Science*, *7*(2), 191643. https://doi.org/10.1098/rsos.191643

Oldham, K. B., Myland, J. C., & Spanier, J. (2009). The hyperbolic tangent tanh(x) and cotangent coth(x) functions. In *An atlas of functions* (pp. 289–296). New York, NY: Springer US. https://doi.org/10.1007/978-0-387-48807-3_31

Österreicher, F., & Vajda, I. (2003). A new class of metric divergences on probability spaces and its applicability in statistics. *Annals of the Institute of Statistical Mathematics*, *55*, 639–653. https://doi.org/10.1007/BF02517812

Palmer, A. N. (1991). Origin and morphology of limestone caves. *GSA Bulletin*, *103*(1), 1–21. https://doi.org/10.1130/0016-7606(1991)103⟨0001:OAMOLC⟩2.3.CO;2

Pareschi, L., & Russo, G. (2005). Implicit-explicit Runge-Kutta schemes and applications to hyperbolic systems with relaxation. *Journal of Scientific Computing*, *25*, 129–155. https://doi.org/10.1007/s10915-004-4636-4

Plummer, L. N., & Wigley, T. M. L. (1976). The dissolution of calcite in CO_2-saturated solutions at 25°C and 1 atmosphere total pressure. *Geochimica et Cosmochimica Acta*, *40*(2), 191–202. https://doi.org/10.1016/0016-7037(76)90176-9

Plummer, L. N., Wigley, T. M. L., & Parkhurst, D. L. (1978). The kinetics of calcite dissolution in CO_2-water system at 5 degrees to 60 degrees C and 0.0 to 1.0 atm CO_2. *American Journal of Science*, *278*, 179–216. https://doi.org/10.2475/ajs.278.2.179

Pogge von Strandmann, P. A. E., Burton, K. W., Snæbjörnsdóttir, S. O., Sigfússon, B., Aradóttir, E. S., Gunnarsson, I., ... Gislason, S. R. (2019). Rapid CO_2 mineralisation into calcite at the CarbFix storage site quantified using calcium isotopes. *Nature Communications*, *10*(1983). https://doi.org/10.1038/s41467-019-10003-8

Prabhakaran, S., & Jones Tarcius Doss, L. (2015). Total variation diminishing finite volume schemes for one-dimensional advection-diffusion equation and

the relationship between flux limiter and mesh parameters. *International Journal of Pure and Applied Mathematics*, *101*, 233–250. Retrieved from https://ijpam.eu/contents/2015-101-2/9/9.pdf https://doi.org/10.12732/ijpam.v101i2.9

Reddy, M. M. (1975). Kinetics of calcium carbonate formation. In *Internationale vereinigung für theoretische und angewandte limnologie: Verhandlungen* (Vol. 19, pp. 429–438). Taylor & Francis. https://doi.org/10.1080/03680770.1974.11896082

Reddy, M. M. (1977). Crystallization of calcium carbonate in the presence of trace concentrations of phosphorus-containing anions: I. inhibition by phosphate and glycerophosphate ions at ph 8.8 and 25°c. *Journal of Crystal Growth*, *41*(2), 287–295. https://doi.org/10.1016/0022-0248(77)90057-4

Rivière, B. (2008). *Discontinuous galerkin methods for solving elliptic and parabolic equations*. Society for Industrial and Applied Mathematics. https://doi.org/10.1137/1.9780898717440

Roe, P. L. (1986). Characteristic-based schemes for the euler equations. *Annual Review of Fluid Mechanics*, *18*, 337–365. https://doi.org/10.1146/annurev.fl.18.010186.002005

Roy, T., Jönsthövel, T. B., Lemon, C., & Wathen, A. J. (2019). A block preconditioner for non-isothermal flow in porous media. *Journal of Computational Physics*, *395*, 636–652. https://doi.org/10.1016/j.jcp.2019.06.038

Saar, M. O. (2011). Review: Geothermal heat as a tracer of large-scale groundwater flow and as a means to determine permeability fields. *Hydrogeology Journal*, *19*, 31–52. https://doi.org/10.1007/s10040-010-0657-2

Shi, D., Brown, P. W., & Ma, W. (1991). Lognormal simulation of pore size distributions in cementitious materials. *Journal of the American Ceramic Society*, *74*, 1861–1867. https://doi.org/10.1111/j.1151-2916.1991.tb07800.x

Shook, G. M. (2001). Predicting thermal breakthrough in heterogeneous media from tracer tests. *Geothermics*, *30*(6), 573–589. https://doi.org/10.1016/S0375-6505(01)00015-3

Subhas, A. V., Rollins, N. E., Berelson, W. M., Dong, S., Erez, J., & Adkins, J. F. (2015). A novel determination of calcite dissolution kinetics in seawater. *Geochimica et Cosmochimica Acta*, *170*, 51–68. https://doi.org/10.1016/j.gca.2015.08.011

Svensson, U., & Dreybrodt, W. (1992). Dissolution kinetics of natural calcite minerals in CO_2-water systems approaching calcite equilibrium. *Chemical Geology*, *100*(1), 129–145. https://doi.org/10.1016/0009-2541(92)90106-F

Sweby, P. K. (1984). High resolution schemes using flux limiters for hyperbolic conservation laws. *SIAM Journal on Numerical Analysis*, *21*, 995–1011. https://doi.org/10.1137/0721062

Teng, H. H., Dove, P. M., & De Yoreo, J. J. (2000). Kinetics of calcite growth: surface processes and relationships to macroscopic rate laws. *Geochimica et Cosmochimica Acta*, *64*(13), 2255–2266. https://doi.org/10.1016/S0016-7037(00)00341-0

van Leer, B. (1985). Upwind-difference methods for aerodynamic problems governed by the Euler equations. In *Large-scale computations in fluid mechanics* (Vol. 22, pp. 327–336).

Vikhansky, A., & Ginzburg, I. (2014). Taylor dispersion in heterogeneous porous media: Extended method of moments, theory, and modelling with two-relaxation-times lattice boltzmann scheme. *Physics of Fluids*, *26*(2), 022104. https://doi.org/10.1063/1.4864631

Virtanen, P., Gommers, R., Oliphant, T. E., Haberland, M., Reddy, T., Cournapeau, D., ... SciPy 1.0 Contributors (2020). SciPy 1.0: Fundamental algorithms for scientific computing in Python. *Nature Methods*, *17*, 261–272. https://doi.org/10.1038/s41592-019-0686-2

Wen, H., & Li, L. (2017). An upscaled rate law for magnesite dissolution in heterogeneous porous media. *Geochimica et Cosmochimica Acta*, *210*, 289–305. https://doi.org/10.1016/j.gca.2017.04.019

Wen, H., & Li, L. (2018). An upscaled rate law for magnesite dissolution in heterogeneous porous media: The role of time and length scales. *Geochimica et Cosmochimica Acta*, *235*, 1–20. https://doi.org/10.1016/j.gca.2018.04.024

White, A. F., & Brantley, S. L. (2003). The effect of time on the weathering of silicate minerals: why do weathering rates differ in the laboratory and field? *Chemical Geology*, *202*, 479–506. https://doi.org/10.1016/j.chemgeo.2003.03.001

Zhang, Y., Benson, D. A., & Baeumer, B. (2008). Moment analysis for spatiotemporal fractional dispersion. *Water Resources Research*, *44*(4), W04424. https://doi.org/10.1029/2007WR006291

Zhao, Z., & Skelton, A. (2014). An assessment of the role of nonlinear reaction kinetics in parametrization of metamorphic fluid flow. *Journal of Geophysical Research: Solid Earth*, *119*, 6249–6262. https://doi.org/10.1002/2014JB011016

Øren, P.-E., & Bakke, S. (2003). Reconstruction of berea sandstone and pore-scale modelling of wettability effects. *Journal of Petroleum Science and Engineering*, *39*(3), 177–199. https://doi.org/10.1016/S0920-4105(03)00062-7